Available online at www.sciencedirect.com

ScienceDirect

Geochimica et Cosmochimica Acta 233 (2018) 33–49

Geochimica et Cosmochimica Acta

www.elsevier.com/locate/gca

Barium isotopic composition of the upper continental crust

Xiao-Yun Nan [a], Hui-Min Yu [a], Roberta L. Rudnick [b], Richard M. Gaschnig [c], Juan Xu [a], Wang-Ye Li [a], Qun Zhang [a], Zhang-Dong Jin [d], Xian-Hua Li [e], Fang Huang [a,*]

[a] *CAS Key Laboratory of Crust-Mantle Materials and Environments, School of Earth and Space Sciences, University of Science and Technology of China, Anhui 230026, China*

[b] *Department of Earth Science and Earth Research Institute, University of California–Santa Barbara, Santa Barbara, CA 93106, United States*

[c] *Department of Environmental, Earth and Atmospheric Sciences, University of Massachusetts Lowell, Lowell, MA 01854, United States*

[d] *State Key Laboratory of Loess and Quaternary Geology, Institute of Earth Environment, Chinese Academy of Sciences, Xi'an 710075, China*

[e] *Institute of Geology and Geophysics, Chinese Academy of Sciences, Beijing 100029, China*

Received 10 August 2017; accepted in revised form 3 May 2018; available online 29 May 2018

Abstract

The upper continental crust (UCC) is an important reservoir of Ba within the Earth. We report high precision (≤±0.05‰, 2SD) Ba isotopic data for 71 samples (including granites, granodiorites, loess, glacial diamictites, and river sediments) to constrain the Ba isotopic composition of the UCC. I-type granites from the Fogang batholith, Southeastern (SE) China, exhibit variable $\delta^{137/134}$Ba (−0.16‰ to 0.01‰), which may be due to isotopic fractionation during the latest stages of magmatic differentiation. The $\delta^{137/134}$Ba of S-type granites from Darongshan-Shiwandashan, SE China (−0.03‰ to 0.11‰) correlate with ε_{Nd} (t), likely reflecting mixing of heterogeneous crustal source materials. Five A-type granites with high SiO_2 contents (~76 wt%) from Nankunshan, SE China have remarkably low $\delta^{137/134}$Ba (−0.47‰ to −0.33‰), which possibly arose from magmatic differentiation or assimilation of crustal materials with light Ba isotopic compositions. Loess from northwestern China has homogeneous $\delta^{137/134}$Ba (−0.02‰ to 0.03‰) that shows no correlation with bulk compositions, sample locations, or degree of chemical weathering, suggesting that loess is representative of the average Ba isotopic composition of the UCC. Three river sediments from northern China have $\delta^{137/134}$Ba similar to that of loess. The $\delta^{137/134}$Ba of glacial diamictites vary with CIA values: those with high CIA (≥60) have heterogeneous $\delta^{137/134}$Ba (−0.19‰ to 0.35‰), while those with low CIA (<60) have $\delta^{137/134}$Ba around 0‰, identical to the values of loess and river sediments, suggesting that Ba isotopes can be fractionated during chemical weathering. In all, samples from the UCC have highly heterogeneous $\delta^{137/134}$Ba, ranging from −0.47‰ to 0.35‰. Using the weighted average of samples in this study, the $\delta^{137/134}$Ba of the UCC is estimated to be 0.00 ± 0.03‰ ($2SD/\sqrt{n}$, $n = 71$), which is similar to the average Ba isotopic composition of the upper mantle, but significantly lower than $\delta^{137/134}$Ba of seawater.

Keywords: Barium isotopes; Granites; Loess; Glacial diamictites; River sediments

1. INTRODUCTION

Barium (Ba) is an alkaline earth metal and a large ion lithophile element (LILE) that is highly incompatible during mantle melting (Pilet et al., 2011). Because of its strong enrichment in the crust, especially the upper continental

* Corresponding author.
E-mail address: fhuang@ustc.edu.cn (F. Huang).

https://doi.org/10.1016/j.gca.2018.05.004
0016-7037/

crust (UCC, ~630 ppm, Rudnick and Gao, 2014) relative to the mantle (~6.9 ppm, Sun and McDonough, 1989), Ba could be a sensitive tracer of crustal recycling. Moreover, because Ba is water soluble and also enriched in ocean floor sediments, it has been used to track contributions of subduction-related fluids to arc magmas (e.g., Hawkesworth and Norry, 1983) or recycled sediments to the mantle (Kuritani et al., 2011; Murphy et al., 2002). Particulate Ba or barite fluxes to the ocean and their accumulation rates in sediments have also been used to reconstruct the paleo-oceanic export productivity (e.g., Schmitz, 1987; Nürnberg et al., 1997; Paytan and Griffith, 2007).

Barium has seven stable isotopes: ^{130}Ba (0.11%), ^{132}Ba (0.10%), ^{134}Ba (2.42%), ^{135}Ba (6.59%), ^{136}Ba (7.85%), ^{137}Ba (11.23%), and ^{138}Ba (71.70%). Barium isotope data are usually expressed as $\delta^{13x/134}Ba = [(^{13x/134}Ba_{sample})/(^{13x/134}Ba_{SRM3104a}) - 1] \times 1000$ in permil (where $x = 7$ or 8, Horner et al., 2015; Nan et al., 2015). Significant Ba isotopic fractionation has been found in natural samples (Miyazaki et al., 2014; Horner et al., 2015; Moynier et al., 2015; Nan et al., 2015; Pretet et al., 2015; Bullen and Chadwick, 2016; Cao et al., 2016; van Zuilen et al., 2016a,b; Bates et al., 2017; Hsieh and Henderson 2017; Bridgestock et al., 2018). For example, $\delta^{137/134}$Ba of seawater varies greatly with depth (Horner et al., 2015; Cao et al., 2016; Bates et al., 2017; Hsieh and Henderson, 2017), and there are large Ba isotopic fractionations between modern seawater and corals ($\Delta^{137/134}Ba_{coral\text{-}seawater} \approx -0.26 \pm 0.14‰$, Pretet et al., 2015). Within the UCC, Ba isotopic fractionation has been observed in igneous rocks and in soil profiles (Miyazaki et al., 2014; Huang et al., 2015; Nan et al., 2015; Bullen and Chadwick, 2016; Gong et al., 2016; van Zuilen et al., 2016a,b). Experimental studies reveal significant Ba isotopic fractionation at low temperature, showing that $BaSO_4$, $BaCO_3$, and $BaMn(CO_3)_2$ preferentially incorporate lighter Ba isotopes relative to aqueous solutions during precipitation (von Allmen et al., 2010; Böttcher et al., 2012; Mavromatis et al., 2016). These studies indicate that Ba isotopes have the potential to track both high and low temperature geochemical processes.

In order to develop Ba isotopes as tracers of recycling, the compositions of Earth's reservoirs need to be evaluated. The UCC is an important reservoir of Ba in the Earth, containing ~15% of the budget of the bulk silicate Earth (calculated using the masses reported in Huang et al., 2013, Ba concentrations of UCC from Rudnick and Gao, 2014, and bulk silicate Earth from McDonough and Sun, 1995). However, the Ba isotopic composition of the UCC is still poorly known. There are only rare data for international rock standards that derive from the UCC reported in the literature (Miyazaki et al., 2014; Nan et al., 2015; van Zuilen et al., 2016a,b). Therefore, a comprehensive investigation of samples from the UCC is warranted.

Two methods have traditionally been used to constrain the composition of the UCC (Rudnick and Gao, 2014). One is to obtain the weighted averages of rocks exposed at the surface (e.g., Clarke, 1889; Clarke and Washington, 1924; Poldervaart, 1955; Shaw et al., 1967, 1976; Eade and Fahrig, 1973; Ronov and Yaroshevsky, 1976; Gao et al., 1992, 1998; Condie, 1993; Borodin, 1999; Hu and Gao, 2008), which is the main method by which major elements and a number of soluble trace element concentrations have been determined for the UCC. The other method is to analyze fine-grained clastic sedimentary rocks, loess, or the fine-grained matrix of glacial diamictites to determine the compositions of insoluble elements (e.g., Goldschmidt, 1933; Taylor and McLennan, 1985; Plank and Langmuir, 1998; Barth et al., 2000; McLennan, 2001; Hu and Gao, 2008; Gaschnig et al., 2016).

Here we present Ba isotopic data for a variety of upper crustal samples, including granites, granodiorites, loess, glacial diamictites, and river sediments, to estimate the average Ba isotopic composition of the UCC. First, we use the weighted average $\delta^{137/134}$Ba of granites (the most important Ba-rich igneous rock types in the UCC), to determine the Ba isotopic composition of the UCC. This method has been used to constrain the average metal stable isotope compositions of the UCC for Li, Mg, Si, Fe, Cu, Mo, and U (e.g., Teng et al., 2004; Li et al., 2009; Li et al., 2010; Savage et al., 2012; Foden et al., 2015; Tissot and Dauphas, 2015; Yang et al., 2017). Second, we determine the Ba isotopic composition of loess, glacial diamictites, and river sediments (see Rudnick and Gao, 2014) and references therein for an explanation of these various UCC proxies, and Gaschnig et al. (2016) for glacial diamictites). Our results reveal significant Ba isotope variations in upper crustal materials, which may reflect Ba isotopic fractionation during magmatic differentiation and chemical weathering. Based on the weighted average $\delta^{137/134}$Ba of the samples in this study, our estimate of Ba isotopic composition of the UCC is $0.00 \pm 0.03‰$ ($2SD/\sqrt{n}$, $n = 71$), which provides a benchmark for applications of Ba isotopes as geochemical tracers.

2. SAMPLES

The UCC is composed of granites, granodiorites, tonalities, gabbros, and metamorphic rocks (Verlag Wedepohl, 1995). The concentration of Ba in gabbros is low (~56 ppm, Field and Elliott, 1974), so the contribution of gabbro to Ba of the bulk UCC is negligible and is therefore not considered further in this study. (Meta)sediments are also important rocks for estimating the average composition of the UCC, with Ba contents ranging from <5 ppm to thousands of ppm (Foster, 1962; Binns, 1967). In particular, loess and diamictites are produced by natural wide-scale sampling, and have been used to derive an average composition of large areas of continental crust. Therefore, we focus our study on granites and sedimentary materials (loess, glacial diamictites and river sediments), which have higher Ba concentrations.

Granites investigated here include I-, S-, and A-type granites and granodiorites from SE China (Li et al., 2007; Qi et al., 2007; Chen et al., 2013). Clastic sediments include loess from northwestern China (Hao et al., 2012; Tsai et al., 2014), globally distributed Precambrian and Paleozoic glacial diamictites (Gaschnig et al., 2014), and sediments from northern China (the correlation plot of Ba and SiO_2 for all samples is provided in Fig. S1).

2.1. Granites

Granites are the most significant host of Ba in the crystalline UCC, and their Ba isotope compositions provide a useful average of the UCC. Moreover, studies of granites provide insight into the isotope composition of their source regions in the middle and lower crust, as demonstrated in previous studies of Li and Mg isotopes (Penniston-Dorland et al., 2017; Teng, 2017, and references therein). To date, Ba isotope data have been published for only two granites, *senu lato* (reference materials G-2, van Zuilen et al., 2016b; GSP-2, Nan et al., 2015). Here, we report data for 23 well-characterized I-, S- and A-type granites and three granodiorites. Although some granites show slight alteration of feldspar, $\delta^{137/134}$Ba seem not correlate with apparent alteration (see petrographic descriptions in the supplementary materials).

2.1.1. I-type granites

Chappell and White (1974, 1992) defined I-type granites as those derived from melting of mantle-derived igneous rocks. We analyzed nine variably differentiated I-type granites from the Fogang Batholith, Guangdong Province, SE China. The ~160 Ma Fogang Batholith, with a total exposed area of ~6000 km^2, is the largest Mesozoic batholith in the Nanling region. The dominant rock types of the Fogang Batholith are coarse-grained biotite monzogranite and syenogranite with K-feldspar megacrysts. They are composed of 25–40% quartz, 25–45% K-feldspar, 20–45% plagioclase (An_{15-35}), 2–8% biotite, 0–5% hornblende, 0–1% muscovite, and trace quantities of zircon, apatite, allanite, titanite, magnetite, and ilmenite (Li et al., 2007).

These granites exhibit large variations in SiO_2 contents (64–77 wt%) (Table 1), low MgO contents, and high total alkali contents. The modified alkali-lime index (MALI (wt %) = $Na_2O + K_2O$-CaO, Frost et al., 2001) of these granites range from 0.48 to 7.56 (Table S1 and Fig. S3). The Alumina Saturation Index (ASI, defined as molar $[Al_2O_3/(CaO + Na_2O + K_2O)]$) range from metaluminous (0.92) to weakly peraluminous (1.07) (Table S1 and Fig. S3 in SOM) (Zen, 1986). The Ba contents of the Fogang granites are also highly variable (35–800 ppm, Table 1) (Li et al., 2007).

2.1.2. S-type granites

S-type granites are interpreted to be derived from partial melting of deep-seated sedimentary rocks (Chappell and White, 1974, 1992, 2001; Chappell and Simpson, 1984). Nine S-type granites from the ~230 Ma Darongshan-Shiwandashan granitoid belt, Guangxi Province, SE China (Qi et al., 2007) were analyzed here. This belt consists of the Pubei pluton, the Jiuzhou pluton, and the Taima pluton, with a total outcrop area of ~10,000 km^2 and distribution over 100 km. These S-type granites intruded into Paleozoic to early Triassic sedimentary strata, and the surrounding rocks are mainly slates, siliceous rocks, sandstones, shales, and carbonates. The major rock types are cordierite biotite granite in the Pubei and Darongshan plutons, cordierite biotite monzogranite in the Jiuzhou pluton, and hypersthene granite porphyry in the Taima pluton. The main minerals include quartz, plagioclase, and biotite, with small amounts of garnet, cordierite, hypersthene, and muscovite. These granites range from calc-alkaline to alkali-calcic types with MALI from 2.56 to 6.35; all are peraluminous with ASI > 1.1 (Table S1 and Fig. S3 in SOM). The SiO_2 contents vary from 65 to 72 wt% and Ba contents from 480 to 830 ppm (Table 1).

2.1.3. A-type granites

A-type granites, as first defined by Loiselle and Wones (1979), generally occur within rift zones or stable continental blocks. Five A-type granites from Nankunshan, SE China were analyzed here. The ~160 Ma Nankunshan A-type granites crop out southeast of the Fogang Batholith over an area of 200 km^2 (Li et al., 2007), and intrude the Middle Jurassic Gaojiping group volcanic rocks. These A-type granites are enriched in K-feldspar crystals, and they contain 23–36% quartz, 24–48% perthite, 14–18% albite (An_{0-5}), 2–5% annite, 0.3–0.5% muscovite, and trace quantity of fluorite (Qi et al., 2007). They are highly evolved with homogenous SiO_2 contents from 76 to 77 wt%, high total alkalis, and exhibit only a small range of major and trace element compositions (Table 1). These granites are alkali-calcic with MALI ranging from 7.53 to 7.81 (Table S1 and Fig. S3 in SOM). Their ASI range from 0.98 to 1.05, corresponding to slightly metaluminous to weakly peraluminous compositions (Table S1 and Fig. S3). Compared to the I- and S-type granites, the Ba concentrations of A-type granites are relatively low (19–56 ppm, Table 1).

2.1.4. Granodiorites

Three granodiorites from the Zhangzhou batholith, SE China were also analyzed here. The Zhangzhou batholith intruded between 97 and 123 Ma ago and is a typical Phanerozoic intrusion that consists of intermediate and silicic igneous rocks (Chen et al., 2013). The granodiorites analyzed here have high Ba concentrations (590–610 ppm) (Table 1). More details of the samples are available in Chen et al. (2013).

2.2. Loess

Loess is wind-blown sediment generally derived from glacial outwash plains and desert regions in cold and dry climates (Taylor et al., 1983). It is mainly comprised of quartz, feldspar, sheet silicates, and/or calcite (Taylor et al., 1983). Because loess samples large continental areas and is mainly produced by mechanical abrasion by glaciers, with limited influence of chemical weathering (Foster, 1947; Smalley and Cabrera, 1970), it has been widely used to estimate the average composition of the UCC (e.g., Taylor et al., 1983; Gallet et al., 1998; Barth et al., 2000; Peucker-Ehrenbrink and Jahn, 2001; Teng et al., 2004; McDaniel et al., 2004; Hu and Gao, 2008; Li et al., 2010; Park et al., 2012; Savage et al., 2013; Chauvel et al., 2014; Sauzéat et al., 2015). No Ba isotope data have yet been reported for loess.

Table 1
Barium isotopic composition of granites and granodiorites.

Sample ID	Ba[a] (ppm)	SiO_2[a] (wt%)	Ba/Th[a]	Rb/Th[a]	I_{Sr}[a]	εNd(t)[a]	$\delta^{137/134}$Ba (‰)[b]	2SD[c]	$\delta^{137/135}$Ba (‰)[b]	2SD[c]	*n*	Method
Fogang I-type granites												
2KSC3	35	76.69	0.8	9.8	0.7116	−10.6	−0.15	0.03	−0.10	0.02	5	D-spike
2KSC76	500	69.01	14.5	7.8	0.7113	−8.6	−0.05	0.05	−0.04	0.03	3	Ce-doping
2KSC79	153	71.58	3.9	8.3	0.7127	−7.4	−0.01	0.03	−0.01	0.02	3	D-spike
Repeat[d]							−0.02	0.03	−0.01	0.02	3	D-spike
P1	795	64.24	55.6	9.4	0.7107	−8.2	−0.01	0.04	−0.01	0.02	3	Ce-doping
P4	636	63.94	35.7	8.3	0.7101	−7.5	0.01	0.04	0.01	0.02	3	Ce-doping
MR42	68	75.35	1.4	11.8	0.7098	−4.3	−0.03	0.04	−0.02	0.03	2	D-spike
Repeat							−0.05	0.03	−0.03	0.02	2	D-spike
2KF396	404	71.35	11.7	8.4	0.7105	−5.6	−0.02	0.04	−0.01	0.03	3	D-spike
Repeat							0.00	0.04	0.00	0.03	1	D-spike
2KGN4-1	136	77.31	3.8	8.5	0.7125	−7.1	−0.15	0.04	−0.10	0.03	3	D-spike
2KGN4-3	179	75.38	3.8	7.9	0.7122	−7.4	−0.14	0.05	−0.09	0.04	3	Ce-doping
Replicate[e]							−0.16	0.04	−0.11	0.01	3	Ce-doping
Darongshan-Shiwandashan S-type granites												
2KD-106	537	69.90	29.6	11.6	0.7272	−12.7	0.03	0.05	0.02	0.03	3	Ce-doping
2KD-110a	552	71.67	30.0	11.6	0.7295	−13.0	0.11	0.05	0.08	0.03	3	Ce-doping
Repeat							0.09	0.04	0.06	0.03	2	D-spike
2KD-122	824	69.62	37.5	10.9	0.7266	−12.5	0.08	0.05	0.05	0.03	3	Ce-doping
2KD-158a	480	65.51	16.9	6.7	0.7221	−11.6	0.08	0.04	0.05	0.02	3	Ce-doping
2KD-159	667	68.25	31.0	10.3	0.7215	−10.6	−0.03	0.04	−0.02	0.02	3	Ce-doping
2KD-160	739	71.21	33.6	12.9	0.7224	−10.6	0.01	0.04	0.01	0.02	3	Ce-doping
Repeat							−0.01	0.03	−0.01	0.02	2	D-spike
2KD-164	780	70.32	32.5	10.0	0.7218	−10.5	0.06	0.05	0.03	0.03	3	Ce-doping
2KD-166	830	69.88	31.4	8.6	0.7223	−10.0	−0.02	0.05	−0.01	0.03	3	Ce-doping
2KD-171	826	71.19	32.7	8.7	0.7232	−9.9	0.01	0.05	0.01	0.03	3	Ce-doping
Nankunshan A-type granites												
2KGN1-1	19	76.12	0.3	11.6	0.7070	−0.9	−0.33	0.04	−0.22	0.03	2	D-spike
2KGN1-3	23	76.81	0.4	13.1			−0.33	0.04	−0.22	0.03	2	D-spike
2KGN1-4	21	76.47	0.4	14.1	0.7059	0.3	−0.35	0.04	−0.24	0.03	2	D-spike
Repeat							−0.37	0.04	−0.25	0.03	2	D-spike
2KGN2-1	56	76.85	0.9	11.7	0.7044	0.2	−0.47	0.04	−0.32	0.03	2	D-spike
2KGN2-2	19	76.76	0.3	12.4	0.7088	−0.8	−0.41	0.04	−0.28	0.03	3	D-spike
Repeat							−0.40	0.04	−0.27	0.03	2	D-spike
Zhangzhou granodiorites												
08JH308	595	65.72	18.6	8.7			0.05	0.03	0.03	0.02	2	D-spike
08JH309	538	64.87	44.8	3.9			0.08	0.03	0.05	0.02	2	D-spike
08JH311	612	62.95	26.6	5.7			−0.02	0.03	−0.01	0.02	2	D-spike

[a] Data are from Li et al. (2007), Qi et al. (2007), and Chen et al. (2013).
[b] $\delta^{137/x}Ba = [(^{137/x}Ba_{sample})/(^{137/x}Ba_{SRM3104a}) - 1] \times 1000$ in permil, x = 134 or 135. For samples in D-spike method, $\delta^{137/135}Ba = \delta^{137/134}Ba * 2/3$.
[c] 2SD = 2 times the standard deviation of the population of the in-house standards in the same sequence.
[d] Repeat = repeat dissolution and chemical purification of individual samples.
[e] Replicate = repeat chemical purification and measurement of different aliquots of a stock solution.

Eighteen loess samples from different areas of northwestern China were investigated here (Hao et al., 2012; Tsai et al., 2014). Eight samples from Yimaguan and four samples from Luochuan were transported by wind from the inland deserts in northern and northwestern China (Liu and Ding, 1998). Six samples from Nileke were transported from western deserts by westerly winds (Ye et al., 1998).

Loess typically shows limited influence of chemical weathering, as reflected by the relatively low chemical index of alteration (CIA). CIA is defined as molar $Al_2O_3/(Al_2O_3 + CaO^* + Na_2O + K_2O)$, where CaO^* refers to the CaO in silicates only (Nesbitt and Young, 1982a,b; McLennan, 1993). The CIA of loess studied here ranges from 57 to 64 with an average of 60 (Table 2). Because un-weathered igneous rocks typically have CIA around 50 ± 5 (Nesbitt and Young, 1982a,b), the loess is likely derived from moderately weathered materials, with illite and smectite as the dominate clay minerals (Gallet et al., 1998; and references therein).

2.3. Glacial diamictites

Glacial diamictites are poorly sorted sedimentary deposits containing particles of angular and rounded clasts of various sizes in a fine-grained matrix. Glacial diamictites

are typically derived from physically eroded soils and bedrock with little evidence of chemical weathering accompanying transport, deposition, and lithification (Nesbitt and Young, 1996). In particular, diamictites derived from continental ice sheets have the potential to cover an expansive provenance. Thus, glacial diamictites provide an important means to assess the average composition of the UCC, as first suggested by Goldschmidt (1933).

We analyzed the fine-grained matrix of 24 glacial diamictite composites from 24 formations spanning four continents and four geological intervals, i.e., Mesoarchean, Paleoproterozoic, Neoproterozoic, and Paleozoic. The formation names, ages, and general locations for these samples are given in Table 3; more sample details, including latitude and longitude of the individual samples comprising the composites, as well as full major and trace elements, O, Pb, Os, and Li isotopes are available in Gaschnig et al. (2014, 2016), Chen et al. (2016) and Li et al. (2016). The CIA values of the diamictites range from 52 to 87 (Table 3), reflecting variable degrees of chemical weathering of the surface sampled by the glaciers. Samples studied here were previously used to investigate chemical weathering and evolution of the UCC (Gaschnig et al., 2014, 2016; Li et al., 2016).

3. ANALYTICAL METHODS

3.1. Dissolution and Chemical purification

High purity acids, produced by double distillation, and 18.2 MΩ cm ultra-pure water were used throughout the dissolution and purification processes. Chemical purification of Ba was performed in an ISO-class six clean room following the method described in Nan et al. (2015). Samples (with ~6 μg Ba for Ce-doping method or ~0.5 μg Ba for double spike method; see details in Section 3.2) were dissolved in 7 ml Teflon® PFA screw-top beakers (Savillex®). Samples containing organic materials were ashed prior to digestion to destroy organic compounds (Kurzweil et al., 2015). Samples were dissolved in a 3:1 (v/v) mixture of

Table 2
Barium isotopic composition of loess and river sediments.

Sample ID	Ba[a] (ppm)	SiO_2[a] (wt%)	K_2O[a] (‰)	$\delta^{137/134}$Ba (‰)[b]	2SD[c]	$\delta^{137/135}$Ba (‰)[b]	2SD[c]	*n*	Method	CIA[d]
Loess Yimaguan, Gansu										
GYZ-XF-110	457	60.52	2.28	0.03	0.04	0.02	0.03	1	D-spike	57
GYZ-XF-432	498	57.39	2.49	−0.02	0.04	−0.01	0.03	1	D-spike	58
GYZ-XF-490	412	56.85	2.32	0.03	0.04	0.02	0.02	3	D-spike	57
Repeat[e]				0.01	0.04	0.01	0.03	1	D-spike	
GYZ-XF-574	572	65.56	2.78	0.02	0.04	0.02	0.02	3	Ce-doping	61
Repeat				0.02	0.04	0.01	0.03	1	D-spike	
GYZ-XF-682	389	51.20	1.92	−0.01	0.04	−0.01	0.03	1	D-spike	58
GYZ-XF-1110	414	56.36	2.06	0.01	0.04	0.01	0.02	3	Ce-doping	58
Repeat				0.01	0.04	0.01	0.03	2	D-spike	
GYZ-XF-1192	415	55.26	2.21	0.01	0.04	0.01	0.03	1	D-spike	60
GYZ-XF-1060	619	66.55	2.77	−0.01	0.04	−0.01	0.03	1	D-spike	63
Loess Luochuan, Shanxi										
XHM14-70	538	71.32	2.51	−0.01	0.04	−0.01	0.03	2	D-spike	64
XHM14-120	492	65.98	2.34	−0.01	0.04	−0.01	0.03	1	D-spike	62
XHM14-200	474	64.64	2.28	−0.01	0.04	−0.01	0.03	1	D-spike	61
XHM14-300	540	64.12	2.42	0.01	0.03	0.01	0.02	2	D-spike	62
Loess Nileke, Xinjiang										
NLK11-220	504	57.32	2.47	−0.01	0.04	−0.01	0.03	1	D-spike	58
Repeat				0.01	0.04	0.01	0.03	2	D-spike	
NLK11-660	536	56.72	2.42	0.01	0.04	0.01	0.03	1	D-spike	60
NLK11-1100	513	56.71	2.39	−0.02	0.04	−0.01	0.03	1	D-spike	59
NLK11-1400	519	57.91	2.49	0.03	0.04	0.02	0.03	1	D-spike	58
NLK11-1700	515	55.24	2.54	−0.02	0.04	−0.01	0.03	1	D-spike	63
NLK11-1900	530	56.69	2.52	−0.01	0.04	−0.01	0.03	1	D-spike	61
River sediments, North China										
11LH02	408	69.10		−0.02	0.04	−0.01	0.03	3	D-spike	57
11YD03	491	70.96		0.03	0.05	0.02	0.03	3	Ce-doping	52
11CB03	535	65.61		−0.04	0.04	−0.03	0.03	2	D-spike	54

[a] Data from Hao et al. (2012) and Tsai et al. (2014).
[b] $\delta^{137/x}Ba = [(^{137/x}Ba_{sample})/(^{137/x}Ba_{SRM3104a}) - 1] \times 1000$ in permil, x = 134 or 135. For samples in D-spike method, $\delta^{137/135}Ba = \delta^{137/134}Ba * 2/3$.
[c] 2SD = 2 times the standard deviation of the population of the in-house standards in the same sequence.
[d] CIA is the chemical index of alteration (CIA = molar $Al_2O_3/(Al_2O_3 + CaO^* + Na_2O + K_2O)$) and CaO^* is in silicate portion only (Nesbitt and Young, 1982a,b; McLennan, 1993).
[e] Repeat = repeat dissolution and chemical purification of individual sample.

Table 3
Barium isotopic composition of glacial diamictite composites.

Sample ID	Stratigraphic unit	Approx age	Location	Ba[a] ppm	SiO_2[a] (wt.%)	$\delta^{137/134}$Ba (‰)[b]	2SD[c]	$\delta^{137/135}$Ba (‰)[b]	2SD[c]	*n*	Method	CIA[d]
Bolivia	Paleozoic	300	South America	400	73.61	−0.02	0.03	−0.02	0.01	3	Ce-doping	68
Dwyka East	Paleozoic	300	Africa	773	67.26	0.08	0.03	0.06	0.01	3	Ce-doping	53
Dwyka West	Paleozoic	300	Africa	254	42.80	0.35	0.03	0.23	0.01	3	Ce-doping	64
Repeat[e]						0.33	0.03	0.22	0.02	2	D-spike	
Newfoundland	Neoproterozoic	570	Newfoundland	689	66.76	0.02	0.05	0.02	0.03	3	Ce-doping	55
Nantuo	Neoproterozoic	630	China	1080	65.15	−0.15	0.05	−0.10	0.03	3	Ce-doping	65
Repeat[e]						−0.18	0.04	−0.12	0.03	2	D-spike	
Gucheng	Neoproterozoic	700	China	924	66.49	0.01	0.05	0.01	0.03	3	Ce-doping	67
Blaubeker	Neoproterozoic	630	Namibia	866	76.85	−0.05	0.05	−0.03	0.03	3	Ce-doping	57
Numees	Neoproterozoic	630	Namibia	611	70.68	0.01	0.05	0.01	0.03	3	Ce-doping	54
Ghaub	Neoproterozoic	630	Namibia	365	32.01	−0.03	0.04	−0.02	0.02	3	Ce-doping	62
Kaigas	Neoproterozoic	700	Namibia	593	63.84	0.05	0.03	0.03	0.01	3	Ce-doping	55
Chuos	Neoproterozoic	700	Namibia	508	47.07	0.00	0.03	0.01	0.01	3	Ce-doping	57
Pocatello	Neoproterozoic	680	Idaho	662	69.29	−0.15	0.03	−0.11	0.01	4	Ce-doping	63
Repeat[e]						−0.19	0.04	−0.13	0.03	3	D-spike	
Konnarock	Neoproterozoic	700	Virginia	795	67.54	0.03	0.03	0.01	0.01	3	Ce-doping	53
Gowganda	Paleoproterozoic	2320	Ontario	408	65.84	−0.05	0.03	−0.04	0.01	3	Ce-doping	55
Bruce	Paleoproterozoic	2330	Ontario	428	67.88	−0.03	0.03	−0.02	0.01	3	Ce-doping	60
Ramsay Lake	Paleoproterozoic	2350	Ontario	368	67.91	0.13	0.03	0.08	0.01	3	Ce-doping	64
Repeat[e]						0.13	0.04	0.09	0.03	1	D-spike	
Bottle Creek	Paleoproterozoic	2350	Wyoming	492	71.01	−0.02	0.04	−0.01	0.03	1	D-spike	57
Makganyene	Paleoproterozoic	2436	Africa	162	56.69	0.04	0.03	0.03*	0.01	3	Ce-doping	87
Duitschland	Paleoproterozoic	2424	South Africa	240	55.09	−0.17	0.04	−0.11	0.33	1	D-spike	81
Timeball Hill	Paleoproterozoic	2310	Africa	326	64.99	−0.06	0.04	−0.04	0.02	3	Ce-doping	66
Mozaan	Mesoarchean	2950	Africa	317	57.24	−0.08	0.03	−0.05	0.02	2	D-spike	72
Afrikander	Mesoarchean	2950	Africa	226	63.28	−0.07	0.04	−0.05	0.04	1	D-spike	77
Coronation	Mesoarchean	2950	Africa	578	72.04	−0.01	0.04	0.01	0.02	3	Ce-doping	78
Replicate[f]						−0.01	0.04	−0.01	0.02	3	Ce-doping	
Promise	Mesoarchean	2950	Africa	287	70.30	0.19	0.04	0.14	0.02	3	Ce-doping	75
Repeat[e]						0.16	0.04	0.11	0.03	1	D-spike	

[a] Data are from Gaschnig et al. (2014) and Gumsley et al. (2017).
[b] $\delta^{137/x}Ba = [(^{137/x}Ba_{sample})/(^{137/x}Ba_{SRM3104a}) - 1] \times 1000$ in permil, x = 134 or 135. For samples in D-spike method, $\delta^{137/135}Ba = \delta^{137/134}Ba * 2/3$.
[c] 2SD = 2 times the standard deviation of the population of the in-house standards in the same sequence.
[d] CIA refers to chemical index of alteration (CIA = molar $Al_2O_3/(Al_2O_3 + CaO^* + Na_2O + K_2O)$) and CaO^* is silicate portion only (Nesbitt and Young, 1982a,b; McLennan, 1993).
[e] Repeat = repeat dissolution and chemical purification of individual sample.
[f] Replicate = repeat chemical purification and measurement of different aliquots of a stock solution.

concentrated HF and HNO_3. After dry down and treating with aqua regia and HCl to remove fluorides, samples were taken up in 3 mol L^{-1} HCl for column separation.

Ba was purified from the matrix using cation exchange columns with AG50W-X12 resin (200–400 mesh, Bio-Rad, USA) following established procedures (Nan et al., 2015). Ba was collected using 4 mol L^{-1} HNO_3 after eluting the matrix elements using 3 mol L^{-1} HCl. The samples were purified twice using a 2 ml resin column followed by the second column using 0.5 ml resin. In this study, an additional column using 0.5 ml AG50W-X12 resin was applied to further separate Ba from rare earth elements. The resin was cleaned with 6 ml 4.5 mol L^{-1} HNO_3 mixed with 0.5 mol L^{-1} HF, followed by 3 ml 18.2 MΩ cm H_2O, and conditioned with 3 ml 2 mol L^{-1} HNO_3. After the samples were loaded with 1 ml 2 mol L^{-1} HNO_3 and rinsed by 5 ml 2 mol L^{-1} HNO_3, Ba was finally collected in 16 ml 2 mol L^{-1} HNO_3. The purified samples were dried down and diluted with 2% (m/m) HNO_3 for instrumental measurement. The yields of the purification process were >99% and the total procedural blank was <5 ng.

3.2. Mass bias correction

Barium isotope compositions were analyzed using a Thermo-Fisher Scientific Neptune-Plus MC-ICP-MS in the CAS Key Laboratory of Crust-Mantle Materials and Environments at the University of Science and Technology of China (USTC). Two methods were used to correct the instrumental mass discrimination.

The first is the Ce-doping method, as Ce has stable isotopes with masses close to Ba isotopes. This elemental doping approach has been used for a number of isotope systems, e.g., Cu and Zn (Maréchal et al., 1999; Archer and Vance, 2004), Fe and Cu (Kehm et al., 2003; Roe et al., 2003), and Tl for Pb (e.g., Hirata, 1996; Belshaw et al., 1998; Rehkämper and Halliday, 1998; Rehkämper and Mezger, 2000). In this method, the purified Ba solution was diluted to ~1.5 ppm with ~120 ppb pure Ce solution. The sensitivity of ^{137}Ba was ~12 V/ppm using a "wet plasma" in low resolution mode. Concentration differences between samples and bracketed standards were less than 20% to avoid analytical artifacts (Nan et al., 2015). ^{134}Ba, ^{135}Ba, ^{136}Ba, ^{137}Ba, ^{140}Ce, ^{142}Ce, and ^{143}Nd were collected on Faraday cups L4, L3, L2, L1, H1, H2, and H3, respectively. ^{143}Nd was monitored to subtract the interference of ^{142}Nd on ^{142}Ce using a linear correction method. The Xe signal was stable in both blanks and samples under wet plasma so that the interference of Xe was not considered here. The "on-perk zero" measurements were conducted before every sequence. The exponential law was used to correct the mass bias on $\delta^{137/134}$Ba, assuming that the fractionation factor (β) of Ce is the same as Ba.

The other calibration method is the double-spike method (D-spike), by which we can analyze samples with low Ba contents (<10 ppm) and further improve the accuracy of $\delta^{137/134}$Ba measurement. In this study, ^{135}Ba and ^{136}Ba were chosen as the double-spike pair with the optimum ratio of 1.72 (m/m) according to Rudge et al. (2009). Due to the absolute high yields of the chemical procedure, the double spike was added after the column separation and a few tests were also performed on solutions where the spikes were added before column separation. The sample/standard solution containing ~100 ng Ba was mixed with an appropriate amount of the ^{135}Ba-^{136}Ba spike solution. The mixed solutions were expected to have a ^{135}Ba/^{134}Ba around 23. A dry plasma using an Aridus II desolvator (CETAC Technologies) was adopted for obtaining higher sensitivity. ^{131}Xe, ^{134}Ba, ^{135}Ba, ^{136}Ba, ^{137}Ba, and ^{140}Ce were collected on Faraday cups L4, L2, L1, C-cup, H1 and H3, respectively. ^{131}Xe and ^{140}Ce were monitored to deduct the interferences of ^{134}Ba and ^{136}Ba, assuming that the fractionation factor (β) was the same as that of Ba. Before the measurement, the sample solutions were diluted to 100 ppb. The background signal in 2% (m/m) HNO_3 for ^{137}Ba (<5 mV) was negligible relative to the sample signals (~7 V).

3.3. Precision and accuracy

In order to evaluate the precision and accuracy of our methods, we analyzed one synthetic standard (SRM3104a mixed with different matrices), two pure Ba standard solutions, i.e., USTC-Ba (an in-house standard purchased from National Standard Material Network) and ICPUS-Ba (an in-house standard purchased from Sigmaaldrich.com), and five rock reference materials.

Barium isotopic compositions for these materials are reported in Table 4. Both the Ce-doping method and double-spike method were used to determine $\delta^{137/134}$Ba of the standards. The external precision of $\delta^{137/134}$Ba, based on the long-term measurements of USTC-Ba and ICPUS-Ba were better than 0.05‰ (2SD) for the Ce doping method, and 0.04‰ (2SD) for double-spike method, respectively. The analyses of the synthetic solutions following integrated column separation yielded average $\delta^{137/134}$Ba of 0.00 ± 0.04‰ (2SD, Ce-doping, Table 4) and 0.01 ± 0.03‰ (2SD, D-spike, Table 4), consistent with the recommended value of 0‰. Barium isotopic compositions of the USGS igneous rock standards BCR-2, G-2, GSP-2, and AGV-1 reported here are within uncertainty of previously published values (Table 4, Nan et al., 2015; van Zuilen et al., 2016a,b). The $\delta^{137/134}$Ba of shale standard SGR-1 is reported here for the first time, 0.11 ± 0.03‰. These data further demonstrate the precision and accuracy of the two methods. Finally, the $\delta^{137/134}$Ba of the reference materials (including synthetic solutions, USTC-Ba, ICPUS-Ba, BCR-2, and G-2) with the spikes added before column separation are consistent with those with spikes added after chemical purification (Table 4), confirming that column chemistry does not generate analytical artifacts for Ba isotopes. Although ^{134}Ce and ^{136}Ce may produce isobaric interferences on ^{134}Ba and ^{136}Ba, respectively, the Ba isotope data are not sensitive to Ce contents of the purified Ba solutions in the double-spike method because the residual Ce was accurately corrected. Tests on USTC-Ba where Ce was added in different concentrations show that the measured $\delta^{137/134}$Ba of USTC-Ba is not affected, even when the Ce/Ba is as high as 0.2 (Fig. 1). Therefore, the influence of ^{134}Ce and ^{136}Ce on Ba isotope measurements of the sam-

Table 4
Barium isotopic composition of reference materials.

Standard	Method	$\delta^{137/134}$Ba (‰)[b]	2SD[c]	n	References
Synthetic Std.[a]	Ce doping	0.00	0.04	8	
	D-spike	0.01	0.03	18	
	D-spike*	-0.01	0.04	2	
USTC-Ba	Ce doping	0.07	0.05	129	
	D-spike	0.06	0.04	81	
Average		0.07	0.04	210	
	D-spike*	0.07	0.03	2	
ICPUS-Ba	Ce doping	-0.02	0.05	104	
	D-spike	-0.03	0.03	80	
Average		-0.02	0.04	184	
	D-spike*	-0.01	0.04	1	
BCR-2	Ce doping	0.04	0.04	3	
	D-spike	0.06	0.03	5	
	D-spike	0.05	0.04	2	
	D-spike	0.05	0.04	2	
Average		0.05	0.03	12	
	D-spike*	0.06	0.04	1	
	SSB#	0.050	0.039	13	Nan et al. (2015)
G-2	Ce doping	0.05	0.05	3	
	Ce doping	0.01	0.03	3	
	D-spike	0.03	0.04	5	
Average		0.03	0.03	11	
	D-spike*	0.03	0.04	1	
	D-spike	0.020	0.030	4	van Zuilen et al. (2016b)
GSP-2	D-spike	0.00	0.03	3	
	SSB#	0.013	0.046	15	Nan et al. (2015)
AGV-1	Ce doping	0.05	0.05	3	
	D-spike	0.05	0.04	1	
Average		0.05	0.03	4	
	SSB#	0.047	0.040	11	Nan et al. (2015)
	D-spike	0.063	0.036	4	van Zuilen et al. (2016b)
SGR-1	Ce doping	0.11	0.04	6	
	Ce doping	0.12	0.04	3	
	D-spike	0.12	0.04	1	
Average		0.11	0.03	10	

D-spike is double-spike. SSB# = the standard-sample bracketing method.
[a] The synthetic standard was made by mixing SRM3104a with matrix elements. The concentration ratio is Al: Fe: Ca: Mg: Na: K: Ba: Sr: La: Ce: Nd = 80: 80: 10: 10: 10: 5: 1: 2.5: 0.5: 0.5: 0.5.
[b] $\delta^{137/134}Ba = [(^{137/134}Ba_{sample})/(^{137/134}Ba_{SRM3104a}) - 1] \times 1000$ in permil.
[c] 2SD = 2 times the standard deviation of the population of the in-house standards in the same sequence.
* Double-spike added before column separation.

ples is negligible because the Ce/Ba in the purified solutions was always <0.01.

4. RESULTS

Barium isotopic compositions are reported in Table 1 for I-, S-, A-type granites, and granodiorites, Table 2 for loess and sediments, Table 3 for glacial diamictites, along with selected chemical compositions (Li et al., 2007; Qi et al., 2007; Hao et al., 2012; Gaschnig et al., 2014; Tsai et al., 2014; Song et al., 2015). Overall, the $\delta^{137/134}$Ba of the UCC materials are highly heterogeneous, ranging from −0.47‰ to 0.35‰ (Fig. 2). The $\delta^{137/134}$Ba of different samples in our study and other reservoirs are shown in Fig. 3.

4.1. Granites

The I-type granites from the Fogang Batholith have $\delta^{137/134}$Ba ranging from −0.16‰ to 0.01‰ with a Ba-weighted average of −0.03 ± 0.14‰ (2SD, $n = 9$). Nine S-type granites from Darongshan-Shiwandashan show $\delta^{137/134}$Ba varying from −0.03‰ to 0.11‰, with a weighted average of 0.03 ± 0.09‰ (2SD, $n = 9$). In contrast to I-type and S-type granites, A-type granites from Nankunshan

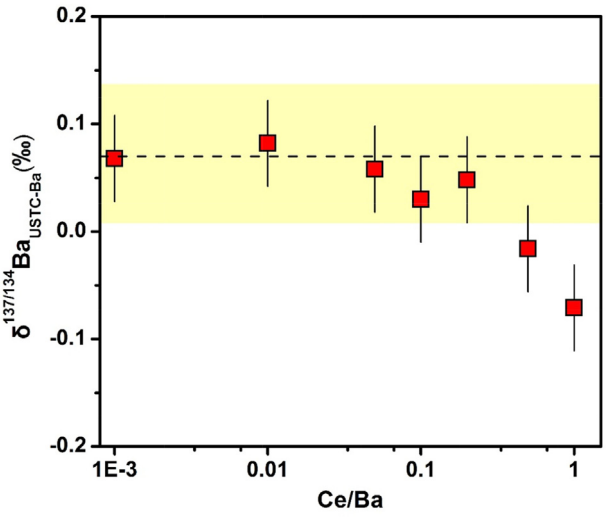

Fig. 1. The effect of Ce content on $\delta^{137/134}$Ba (‰) of a pure Ba standard solution (USTC-Ba) measured by the double spike method. The yellow field represents the recommended $\delta^{137/134}$Ba of USTC-Ba (0.07 ± 0.04‰) and the black dashed line represents the average $\delta^{137/134}$Ba of USTC-Ba (0.07‰). Error bars represent 2SD uncertainties. The measured $\delta^{137/134}Ba_{USTC\text{-}Ba}$ is consistent with the recommended value when Ce/Ba is below 0.2. Ce/Ba in the purified solutions of samples in this study were always below 0.01. (For interpretation of the references to colour in this figure legend, the reader is referred to the web version of this article.)

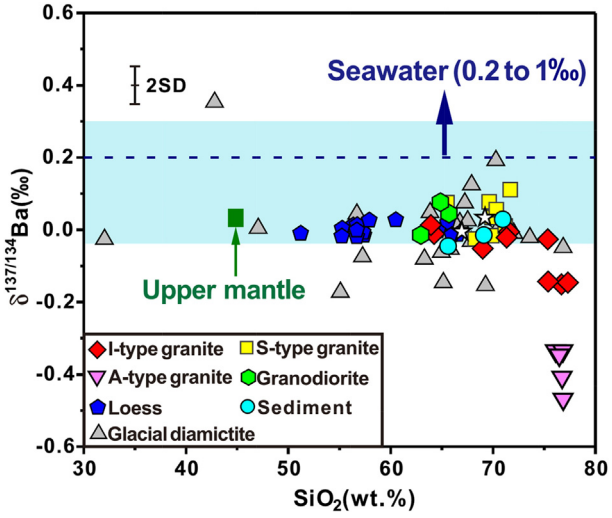

Fig. 2. $\delta^{137/134}$Ba (‰) vs. SiO_2 (wt.%) for all samples in this study. The two stars represent the granite reference materials (G-2 and GSP-2). The arrow represents $\delta^{137/134}$Ba of seawater (0.2‰ to 1.0‰, Horner et al., 2015; Cao et al., 2016; Bates et al., 2017; Hsieh and Henderson 2017). The blue shaded area represents $\delta^{137/134}$Ba of rivers, (−0.04‰ to 0.30‰, Cao et al., 2016). The green square represents the upper mantle (0.020 ± 0.021‰, 2SE, Huang et al., 2015). Error bars represent 2SD uncertainties. Most sediments and rocks have lighter Ba isotopic compositions relative to seawater. Data are from Tables 1–3. (For interpretation of the references to colour in this figure legend, the reader is referred to the web version of this article.)

have lower $\delta^{137/134}$Ba (−0.47‰ to −0.33‰), with a concentration-weighted average of -0.40 ± 0.11‰ ($n = 5$). Three granodiorites from the Zhangzhou batholith have relatively homogeneous $\delta^{137/134}$Ba (−0.02‰ to 0.08‰).

4.2. Loess and river sediments

The $\delta^{137/134}$Ba of loess samples from Yimaguan, Luochuan, and Nileke range from −0.02‰ to 0.03‰; −0.01‰ to 0.01‰; and −0.02‰ to 0.03‰, respectively. These results demonstrate that Ba isotopic compositions are homogenous in loess, regardless of the different sample locations and elemental compositions (Fig. 2). The weighted average $\delta^{137/134}$Ba of loess is 0.00 ± 0.03‰ (2SD, $n = 18$). Three river sediments from North China also have a uniform $\delta^{137/134}$Ba (−0.04‰ ~ 0.03‰), identical to the loess data.

4.3. Glacial diamictites

Glacial diamictite composites show the largest variation among the samples investigated here with $\delta^{137/134}$Ba ranging from −0.19‰ to 0.35‰. The weighted average is nonetheless close to that of loess at -0.01 ± 0.22‰ ($n = 24$, Fig. 2). Four Mesoarchean samples show a relatively large variation in $\delta^{137/134}$Ba (−0.08‰ to 0.19‰), a range similar to that of seven Paleoproterozoic samples (−0.17‰ to 0.13‰). Ten Neoproterozoic and three Paleozoic samples have relatively small variations in $\delta^{137/134}$Ba, ranging from −0.19‰ to 0.05‰ and −0.02‰ to 0.08‰, respectively. One Paleozoic composite, Dwyka West, has an abnormally high $\delta^{137/134}$Ba (0.35‰). This formation is unique among the Paleozoic samples as its detrital zircon population is exclusively >2.0 Ga, and its transition metal and other geochemical signatures indicate a mainly Archean or Paleoproterozoic provenance (Gaschnig et al., 2016).

5. DISCUSSION

The highly variable $\delta^{137/134}$Ba of the UCC materials reported here reflects Ba isotopic fractionation during crustal processes, including magmatism and chemical weathering. In the following sections, we evaluate these processes and then use the data to constrain the average Ba isotopic composition of the UCC.

5.1. Ba isotopic fractionation in granites

5.1.1. I-type granites

Ba isotopic variation is observed in the nine Fogang I-type granites, which have a wide range of chemical compositions. Because Ba is soluble in magmatic fluids, it is necessary to consider whether magmatic fluid phase exsolution during late-stage magmatic differentiation affected the Ba content and Ba isotopic composition of the Fogang granites. To do this, we examine Rb and Th, which have similar incompatibility to one another during granite differentiation, but different fluid solubility, as Rb is more soluble than Th in crustal fluids (Taylor and McLennan, 1985). The constant Rb/Th during differentiation (Fig. 4a) is

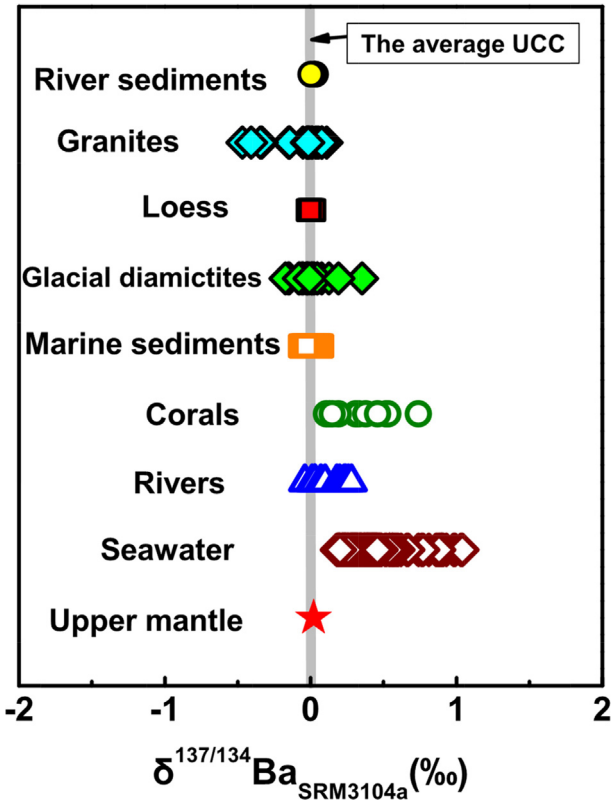

Fig. 3. Summary of $\delta^{137/134}Ba_{SRM3104a}$ (‰) of natural reservoirs. Data source: Marine sediments, Bridgestock et al. (2018); Corals, Pretet et al. (2015); Rivers, Cao et al. (2016); Seawater, Horner et al. (2015), Cao et al. (2016), Bates et al. (2017) and Hsieh and Henderson (2017); and upper mantle, Huang et al. (2015).

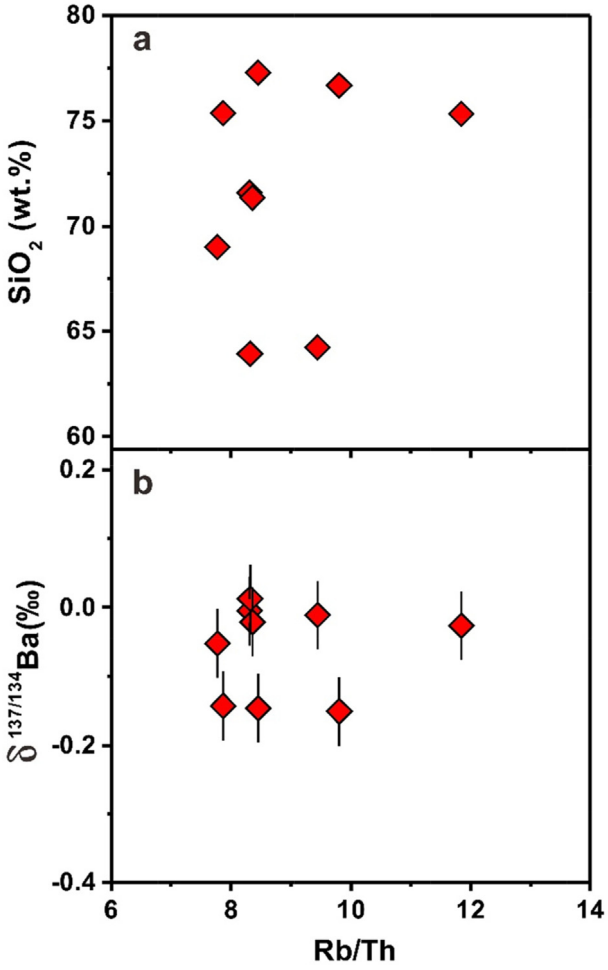

Fig. 4. Rb/Th vs. (a) SiO_2 (wt%), and (b) $\delta^{137/134}Ba$ (‰) for I-type granites analyzed from the Fogang batholith. There is no correlation between "fluid indices" (Rb/Th) and $\delta^{137/134}Ba$ for these granites. Error bars represent 2SD uncertainties. Data are from Table 1.

consistent with their similar incompatibility, and suggests little influence from fluid exsolution. Furthermore, there is no correlation between $\delta^{137/134}Ba$ and Rb/Th (Fig. 4b). Therefore, the effect of fluid activity (if any) on Ba content and Ba isotopic compositions in these granites is not further considered.

Another possible explanation for the variable $\delta^{137/134}Ba$ in these I-type granites is source heterogeneity. Although these granites were suggested to be generated by partial melting of Paleoproterozoic mafic-intermediate igneous protoliths, and mixing with variable amounts of mantle melts (Bao et al., 2000; Li et al., 2007; Xu et al., 2007), Ba isotopic composition is not correlated with ε_{Nd} (t) (Fig. 5b). Thus, source heterogeneity is unlikely to explain the observed Ba isotopic variation in the I-type granites.

Previous work has suggested that the Fogang granites experienced significant fractional crystallization during their formation, as indicated by obvious depletions of Ba, Sr, and Eu relative to the average upper crust values (Li et al., 2007). Whereas both Ba and Sr decrease with increasing SiO_2 (Fig. 6a and b), K_2O first increases, and then decreases at SiO_2 above 72% (Fig. 6c). The K_2O variation may be explained by fractionation of plagioclase and a small amount of K-bearing minerals (such as biotite and K-feldspar) during the early stages of the differentiation (e.g., Blundy and Wood, 1991), and then separation of plagioclase and more K-bearing minerals during the later stages of differentiation (e.g., Philpotts and Schnetzler, 1970; Ewart and Griffin, 1994). The $\delta^{137/134}Ba$ of the I-type granites do not show a linear correlation with SiO_2 (Fig. 6d) or Ba contents (Fig. 5a), but there is a general trend of lower $\delta^{137/134}Ba$ with differentiation (i.e., as SiO_2 rises and Ba ppm decreases). Most samples have similar $\delta^{137/134}Ba$ within analytical uncertainty (0.05‰, 2SD) except for the three samples having high-SiO_2, low K_2O, low Ba, and low $\delta^{137/134}Ba$ (Fig. 6d). These low values may reflect separation of Ba-rich minerals (e.g., biotite and/or K-feldspar) that are enriched in heavy Ba isotopes during the latest stages of granite differentiation (where $SiO_2 \approx 75\%$). Rayleigh distillation calculations provide an estimate of the Ba isotope fractionation factor (α) during Ba-rich mineral (e.g., K-feldspar, biotite, etc.) fractional crystallization (Fig. 7). Assuming that the $\delta^{137/134}Ba$ of the starting melt was 0, α between Ba-rich mineral and melt is estimated to range from 1.000005 to 1.00005.

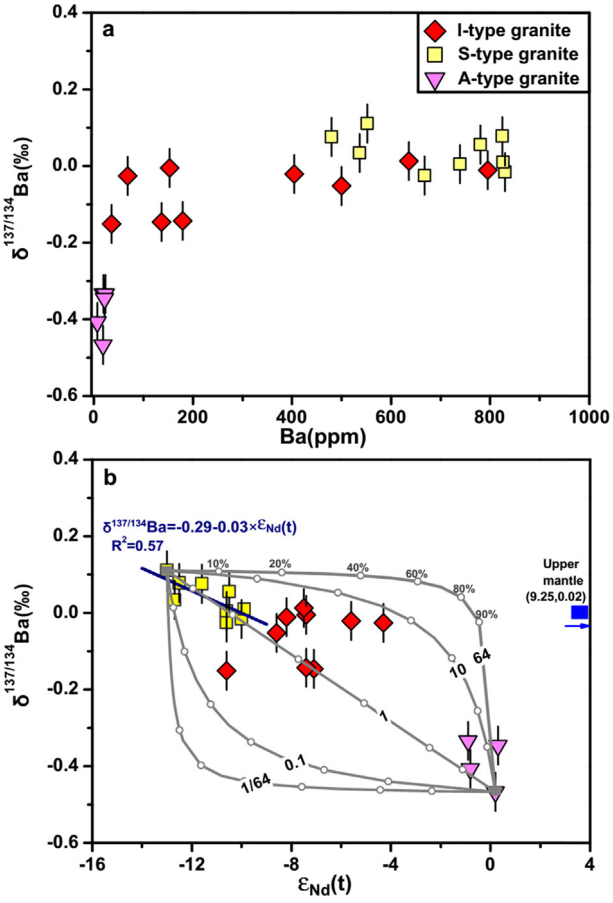

Fig. 5. (a) $\delta^{137/134}$ Ba (‰) vs. Ba (ppm) and (b) $\delta^{137/134}$ Ba (‰) vs. ε_{Nd} (t) for I-, S-, and A-type granites in this study. The negative correlation for S-type granites from Darongshan-Shiwandashan (dark blue line) reflects mixing of heterogeneous sources. A binary mixing model is applied to model the Ba isotopic variability. The mixing end-members are based on data measured in this study, i.e., A-type granite (ε_{Nd} (t) of 0.2 and $\delta^{137/134}$ Ba of −0.47‰), and the most evolved S-type granite (ε_{Nd} (t) of −13 and $\delta^{137/134}$ Ba of 0.11‰). The $(Ba/Nd)_{S\text{-granite}}/(Ba/Nd)_{A\text{-granite}}$ is set at 64. We varied the ratios of $(Ba/Nd)_{S\text{-granite}}$ and $(Ba/Nd)_{A\text{-granite}}$ to achieve a range of $(Ba/Nd)_{S\text{-granite}}/(Ba/Nd)_{A\text{-granite}}$ (10, 1, 1/10, and 1/64) in order to determine the effect of this ratio on Ba isotope compositions of granites (gray curves). The blue square represents the average upper mantle with ε_{Nd} (t) = 9.25 (White and Klein, 2014) and $\delta^{137/134}$ Ba = 0.02 ± 0.02‰ (Huang et al., 2015). Error bars represent 2SD long-term precision of ±0.05‰. Data are from Table 1. (For interpretation of the references to colour in this figure legend, the reader is referred to the web version of this article.)

5.1.2. S-type granites

Nine S-type granites from three different supersuites of the Triassic Darongshan-Shiwandashan belt are highly evolved, with high SiO_2 contents (Fig. 2). Their high I_{Sr} (initial Sr isotopic composition, >0.721) and low ε_{Nd} (t) (−13.0 to −9.9) values (Qi et al., 2007) suggest that these S-type granites formed from re-melting of older crustal materials. There is no correlation between $\delta^{137/134}$Ba and Ba (Fig. 5a) or SiO_2 contents (Fig. 2), but $\delta^{137/134}$Ba is clearly negatively correlated with ε_{Nd} (t) (Fig. 5b). Such correlation suggests that the higher $\delta^{137/134}$Ba may be contributed by sources with older model ages. It is therefore likely that the Ba isotope variation in these S-type granites reflect mixing between different protoliths.

5.1.3. The low $\delta^{137/134}$Ba in A-type granites

In contrast to the I-type and S-type granites studied here, A-type granites from Nankunshan have lower $\delta^{137/134}$Ba ranging from −0.47‰ to −0.33‰ (Fig. 2). The I_{Sr} (0.706 ± 0.012) and ε_{Nd}(t) (0.3 to −0.9) values for the Nankunshan A-type granites suggest that they might be derived from differentiation of mantle-derived alkaline parental magma involving significant fractional crystallization and assimilation of evolved crustal components (Li et al., 2007). They are all highly differentiated, with homogenous, high SiO_2 contents and very low Ba contents (from 19 to 56 ppm). With our current data, it is not clear whether fractional crystallization or fluid exsolution led to these very light Ba isotopic compositions. Considering their extremely low Ba contents and light Ba isotope compositions (features shared with the most highly differentiated Fogang I-type granites), the low $\delta^{137/134}$Ba in these A-type granites may have also formed from fractionation of a K-bearing phase (biotite and/or K-feldspar) during late stage differentiation. Alternatively, it is also possible that the low $\delta^{137/134}$Ba of these A-type granites may be due to assimilation of crustal components enriched in light Ba isotopes, although such low $\delta^{137/134}$Ba has yet to be observed in the limited data currently available for crustal rocks. Systematic measurements of additional A-type granites may be helpful to understand the fractionation mechanism for Ba isotopes.

Based on the Nd isotope data, A-type granites have experienced the least amount of contamination by crust materials, while S-types have experienced the most contamination, and I-types are intermediate between the A and S types. A binary mixing model was used to examine the effects of crustal contamination on Ba isotope composition for these granites (Fig. 5b). However, none of these mixing curves are consistent with the observed Ba isotope variations.

5.2. Homogeneous Ba isotope composition in loess and river sediments

Loess samples from Yimaguan and Luochuan from the Loess Plateau in Northwestern China mainly formed under arid and semi-arid conditions. Although the loess and associated paleosol layers in these regions reflect varying climatic conditions, their CIA values are all lower than 65 (Fig. 8a), implying that they have experienced limited chemical weathering (McLennan, 1993). Previous studies demonstrated that loess from the Chinese Loess Plateau were derived from rocks that likely experienced incipient weathering during which Ca and Na were leached out, but most of the original K was retained in the soil (Nesbitt and Markovics 1980; Gu et al., 1997; Chen et al., 1998). Ba is generally hosted in K-bearing minerals such as feldspars and micas, and this is supported by the positive correlation between Ba and K in loess (Fig. 9). Therefore, Ba may not be a mobile element during loess formation (Chen et al.,

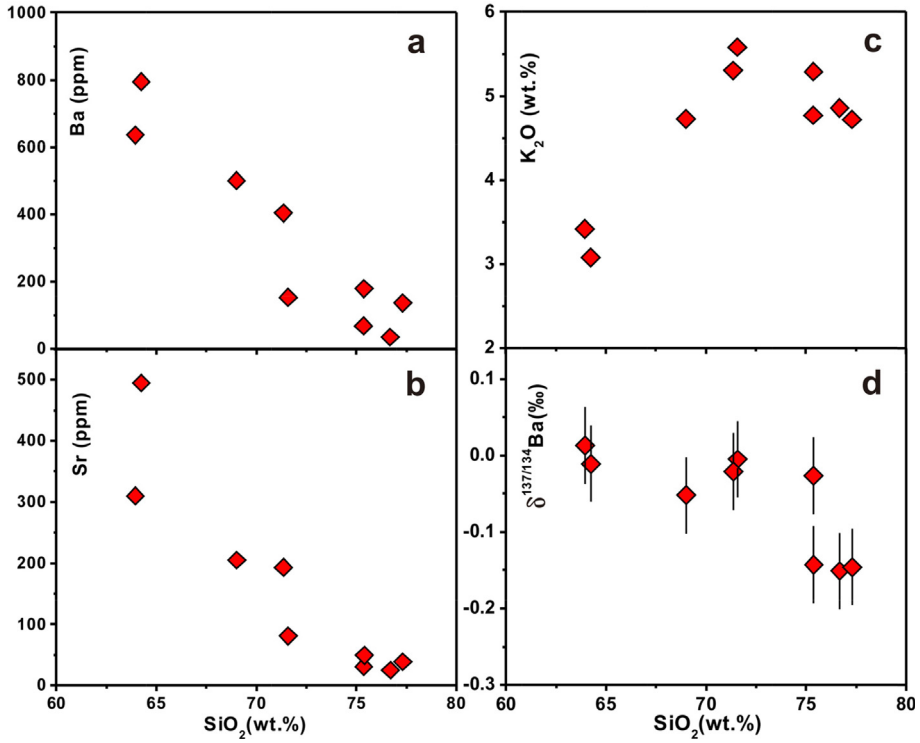

Fig. 6. (a) Ba (ppm) vs. SiO_2 (wt%), (b) Sr (ppm) vs. SiO_2 (wt%), (c) K_2O (wt%) vs. SiO_2 (wt%) and (d) $\delta^{137/134}$Ba (‰) vs. SiO_2 (wt%) for I-type granites from the Fogang batholith. Error bars represent 2SD uncertainties. Data are from Table 1.

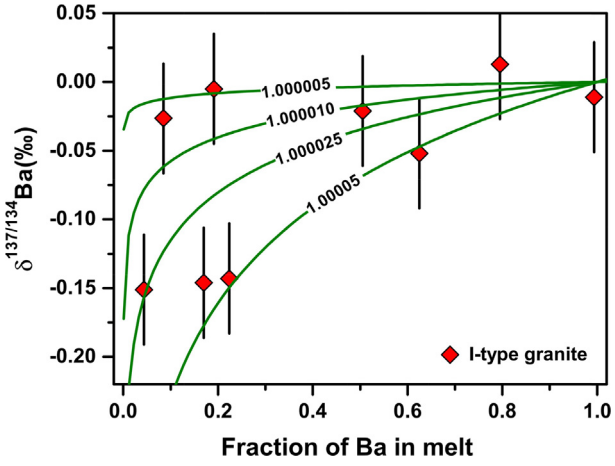

Fig. 7. Rayleigh distillation model of Ba isotope fractionation during Ba-rich mineral (e.g., K-feldspar, biotite, etc.) fractional crystallization. A $\delta^{137/134}$Ba of 0 was used as the starting melt composition. Curves represent different fractionation factors (α) between Ba-rich minerals (e.g., K-feldspar, biotite) and melt.

1998). All loess samples studied here have quite homogenous $\delta^{137/134}$Ba (−0.02‰ to 0.03‰; Fig. 2) with a weighted average of 0.00 ± 0.03‰ (2SD, $n = 18$), regardless of their sample location, chemical compositions, and degree of weathering. Thus, loess can be used to constrain the Ba isotopic composition of the UCC.

Three river sediments from North China have homogenous and similar $\delta^{137/134}$Ba as loess, with their CIA values all <60 (Fig. 8a). The weighted average of $\delta^{137/134}$Ba is −0.01 ± 0.06‰ (2SD, $n = 3$), consistent with the estimate of the averaged $\delta^{137/134}$Ba of the UCC based on loess and granites.

5.3. Ba isotopic variation in glacial diamictites

Glacial diamictites provide an alternative method to assess the average composition of the UCC because they mainly formed by physical weathering (Goldschmidt, 1933). However, in contrast to the homogeneous $\delta^{137/134}$Ba of loess and river sediments, ancient glacial diamictites show a wide range of $\delta^{137/134}$Ba from −0.19‰ to 0.35‰ (Fig. 2). The Ba isotope data for the glacial diamictites are complicated. Whereas major and trace element data suggest a greater component of mafic rocks in the source region of the Archean samples (Gaschnig et al., 2016), incorporation of such materials is unlikely to lead to significant Ba isotope fractionation, as Ba should be incompatible during mafic magmatism, and thus, not result in Ba isotope fractionation. Although $\delta^{137/134}$Ba is not clearly correlated with CIA (Fig. 8a) or the depositional age (Fig. 10), $\delta^{137/134}$Ba shows a larger dispersion (−0.17 ~ 0.35‰) for samples with low Ba contents (≤400 ppm) and high CIA (CIA ≥ 60) (Fig. 8b). By contrast, diamictites with high Ba contents (>400 ppm) and low CIA (CIA < 60) (Fig. 8b) show a smaller range in $\delta^{137/134}$Ba (around 0‰), similar to the values of loess and river sediments, suggesting that both Ba contents and $\delta^{137/134}$Ba can be influenced by chemical weathering. Li et al. (2016) found that

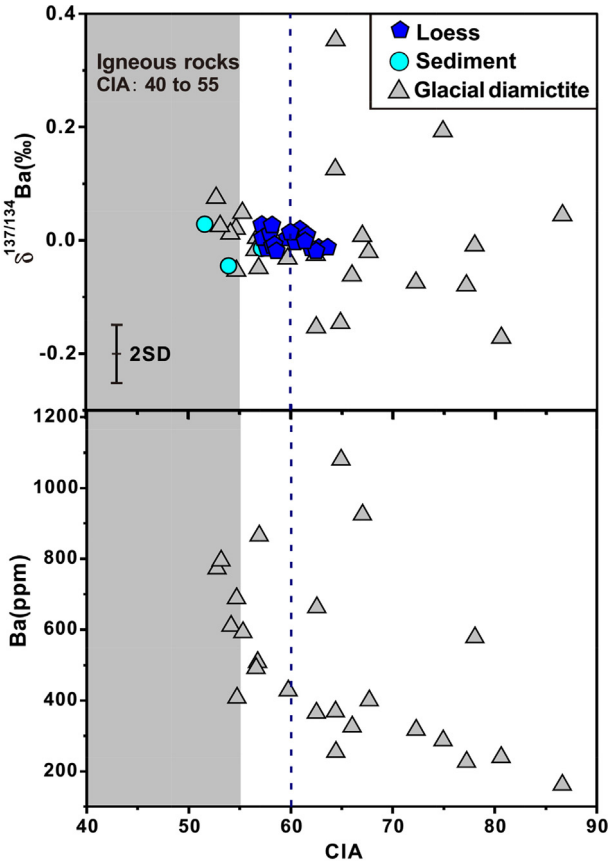

Fig. 8. (a) Variation of $\delta^{137/134}$Ba (‰) vs. CIA for loess, river sediments, and glacial diamictites analyzed in this study. (b) Ba (ppm) vs. CIA for glacial diamictites. Low CIA (<60) suggests weak chemical weathering, whereas high CIA (≥60) reflects moderate to high degree of chemical weathering. The gray shaded area represents fresh igneous rocks with CIA ranging from 40 to 55 (Nesbitt and Young, 1982a,b). Error bars represent 2SD uncertainties. Data are from Tables 2 and 3.

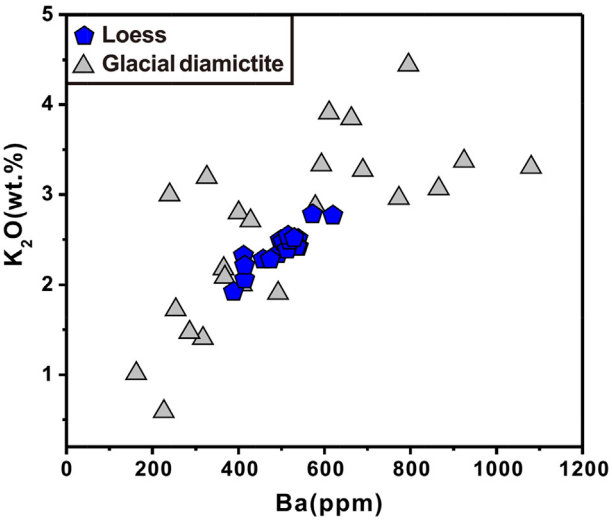

Fig. 9. K_2O (wt%) vs. Ba (ppm) for loess and glacial diamictites in this study. The positive correlation between the Ba and K_2O contents suggests the chemical affinity for these two large ion lithophile elements in sediments. Data are from Tables 2 and 3.

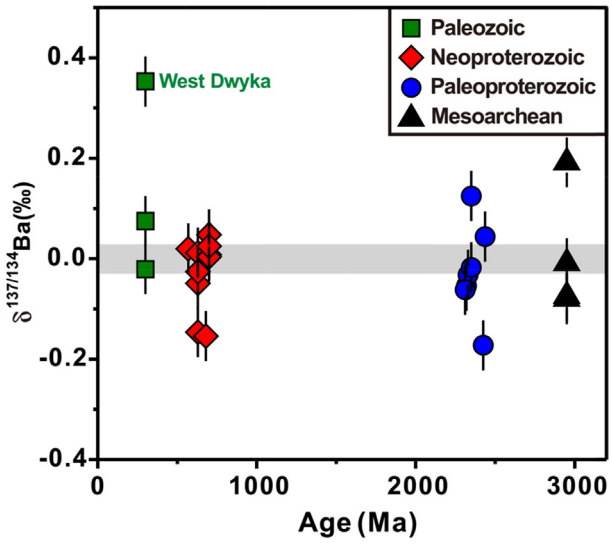

Fig. 10. The $\delta^{137/134}$Ba (‰) vs. ages of glacial diamictites analyzed in this study. The gray band represents the weighted average $\delta^{137/134}$Ba of the UCC (0.00 ± 0.03‰, 2SD/$\sqrt{n}$) obtained here. The $\delta^{137/134}$Ba do not show any clear correlation with the depositional ages of the diamictites, although more ancient diamictites tend to have more variable values, including the West Dwyka sample that has an Archean provenance. Error bars represent 2SD uncertainties. Data are from Table 3.

the weathering signatures recorded in the diamictites were mainly inherited from the UCC that the glaciers traversed. Thus, Ba isotope data of these glacial diamictites may reflect weathering characteristics of the source rocks, and the larger Ba isotope fractionations represent more intensive weathering in the provenance of the diamictites, which tends to occur in the oldest samples. One Paleozoic diamictite (West Dwyka) has very high $\delta^{137/134}$Ba (0.35‰) and also has a Paleoproterozoic to Archean provenance, as reflected in the ages of the detrital zircons (Gaschnig et al., 2016). This suggests that its heavy Ba isotopic composition may be inherited from ancient weathered crust. Ba is positively correlated with K in the glacial diamictites, indicating that Ba is also enriched in K-rich minerals similar to the case in loess (Fig. 9).

The weighted average $\delta^{137/134}$Ba for high Ba glacial diamictite composites (>400 ppm) is -0.02 ± 0.13‰ (2SD, $n = 12$) and low Ba samples (≤400 ppm) is 0.01 ± 0.27‰ (2SD, $n = 12$), which are essentially identical to the estimates of the UCC based on granites, loess, and river sediments. Given the inferred large effects of chemical weathering on Ba isotope fractionation, the glacial diamictites with low CIA provide a better estimate of the average $\delta^{137/134}$Ba of the UCC than those with high CIA.

5.4. Barium isotopic composition of the UCC

The dataset reported in this study reveals that UCC materials have heterogeneous $\delta^{137/134}$Ba, with a range from

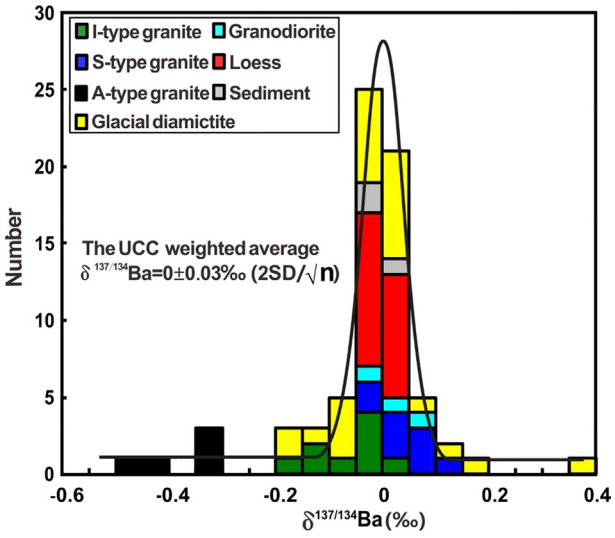

Fig. 11. Histogram of $\delta^{137/134}$Ba values of all samples in this study. The weighted average Ba isotopic composition of the UCC is 0.00 ± 0.03‰ 2SD/$\sqrt{n}$). Data are from Tables 1–3.

−0.47‰ to 0.35‰ (Fig. 2). Two approaches are used here to constrain the average $\delta^{137/134}$Ba of the UCC. First, we calculate the Ba-weighted average of all the granites and granodiorites studied here, which yields an average $\delta^{137/134}$Ba of 0.01 ± 0.07‰ (2SD/$\sqrt{n}$, $n = 26$). A-type granites from SE China have extremely light Ba isotopic compositions, but they do not significantly change the average $\delta^{137/134}$Ba of the UCC because their Ba contents are quite low (<60 ppm). Second, we calculate the Ba-weighted average $\delta^{137/134}$Ba of fine-grained clastic sediments including loess, river sediments, and glacial diamictite composites, which is 0.00 ± 0.02‰ (2SD/$\sqrt{n}$, $n = 45$). This value is the same, within uncertainty of the average $\delta^{137/134}$Ba derived from the granites. Integrating these two methods, the weighted average of all UCC samples studied here is $\delta^{137/134}$Ba = 0.00 ± 0.03‰ (2SD/$\sqrt{n}$, $n = 71$). When plotted on a histogram, the data reported in this study show a peak centered at 0.00‰ (Fig. 11), which represents the best estimate of the average Ba isotopic composition of the UCC. This value is also consistent with the $\delta^{137/134}$Ba estimated for the upper mantle (0.020 ± 0.021‰, 2SE, Huang et al., 2015).

Barium is generally mobile during continental weathering and easily adsorbed by clays, hydroxides, and organic matter. Thus, Ba can be transported from the continents to the oceans in adsorbed or dissolved forms (Puchelt, 1967). The Ba isotopic characteristics of the UCC can provide insights into such processes. Based on results in this study and the literature, although the UCC samples have highly variable Ba isotope compositions (Fig. 3), most of them are lighter than the seawater, with $\delta^{137/134}$Ba ranging from 0.2‰ to 1.0‰ (Horner et al., 2015; Nan et al., 2015; Pretet et al., 2015; Cao et al., 2016; Bates et al., 2017; Hsieh and Henderson, 2017; Bridgestock et al., 2018). Our data reveal that Ba isotopes can be fractionated during continental weathering and water-rock interactions. Although Ba isotope data for water and rock samples have been increasingly reported, application of Ba isotopes to geochemical studies is still in the early stages. Future studies of weathering profiles or river-rock systems will be helpful to decipher Ba cycles between the UCC and the ocean.

6. CONCLUSIONS

The $\delta^{137/134}$Ba of I-type granites from the Fogang batholith vary from −0.16‰ to 0.01‰. The $\delta^{137/134}$Ba of S-type granites from Darongshan-Shiwandashan ranges from −0.03‰ to 0.11‰ and are negatively correlated with ε_{Nd} (t), while A-type granites from Nankunshan have quite low $\delta^{137/134}$Ba (−0.47‰ to −0.33‰). The large variations of $\delta^{137/134}$Ba in granites may reflect fractionation of Ba-rich minerals (particularly during the last stages of differentiation), as well as assimilation of crustal materials enriched in light Ba isotopes. Loess have homogeneous $\delta^{137/134}$Ba with an average of 0.00 ± 0.03‰ (2SD, $n = 18$), regardless of the geography and CIA values. Loess therefore can be used to constrain the average Ba isotopic composition of the UCC. Glacial diamictite composites display a large range of $\delta^{137/134}$Ba (−0.19‰ to 0.35‰). In particular, samples with low Ba and high CIA have highly variable $\delta^{137/134}$Ba, suggesting that Ba isotopes are fractionated during chemical weathering. Overall, the UCC has a heterogeneous Ba isotopic composition with an average $\delta^{137/134}$Ba = 0.00 ± 0.03‰ (2SD/$\sqrt{n}$, $n = 71$), which is similar to the upper mantle, but significantly lighter than oceans and river waters.

ACKNOWLEDGEMENTS

We thank Eva Stüeken, Francois Tissot, and Paolo Sossi for constructive review comments, and Nicolas Dauphas for editorial handling. This work is financially supported by the Chinese National Key R&D Program of the MOST (NO. 2016YFC0600404), the National Science Foundation of China (41630206, 41571130052, 41325011), the 111 Project, and NSF grant EAR-1321954 to RLR and RMG.

APPENDIX A. SUPPLEMENTARY MATERIAL

Supplementary data associated with this article can be found, in the online version, at https://doi.org/10.1016/j.gca.2018.05.004.

REFERENCES

Archer C. and Vance D. (2004) Mass discrimination correction in multiple-collector plasma source mass spectrometry: an example using Cu and Zn isotopes. *J. Anal. Atom. Spectrom.* **19**, 656–665.

Böttcher M. E., Geprägs P., Neubert N., Von Allmen K., Pretet C., Samankassou E. and Nägler T. F. (2012) Barium isotope fractionation during experimental formation of the double carbonate BaMn $[CO_3]_2$ at ambient temperature. *Isot. Environ. Health Stud.* **48**, 457–463.

Bao Z., Zhao Z. and Xiong X. (2000) Geochemistry of Ejinao alkali syenite and its geodynamic significance. *Geochimica* **29**, 462.

Barth M. G., McDonough W. F. and Rudnick R. L. (2000) Tracking the budget of Nb and Ta in the continental crust. *Chem. Geol.* **165**, 197–213.

Bates S. L., Hendry K. R., Pryer H. V., Kinsley C. W., Pyle K. M., Woodward E. M. S. and Horner T. J. (2017) Barium isotopes reveal role of ocean circulation on barium cycling in the Atlantic. *Geochim. Cosmochim. Acta* **204**, 286–299.

Belshaw N., Freedman P., O'nions R., Frank M. and Guo Y. (1998) A new variable dispersion double-focusing plasma mass spectrometer with performance illustrated for Pb isotopes. *Int. J. Mass Spectrom.* **181**, 51–58.

Binns R. A. (1967) Barroisite-bearing Ecologite from Naustdal, Song og Fjordane. *Norway. J. Petrol.* **8**, 349–371.

Blundy J. D. and Wood B. J. (1991) Crystal-chemical controls on the partitioning of Sr and Ba between plagioclase feldspar, silicate melts, and hydrothermal solutions. *Geochim. Cosmochim. Acta* **55**, 193–209.

Borodin L. (1999) Estimated chemical composition and petrochemical evolution of the upper continental crust. *Geochem. Int.* **37**, 723–734.

Bridgestock L., Hsieh Y. T., Porcelli D., Homoky W. B., Bryan A. and Henderson G. M. (2018) Controls on the barium isotope compositions of marine sediments. *Earth Planet. Sci. Lett.* **481**, 101–110.

Bullen T. and Chadwick O. (2016) Ca, Sr and Ba stable isotopes reveal the fate of soil nutrients along a tropical climosequence in Hawaii. *Chem. Geol.* **422**, 25–45.

Cao Z., Siebert C., Hathorne E. C., Dai M. and Frank M. (2016) Constraining the oceanic barium cycle with stable barium isotopes. *Earth Planet. Sci. Lett.* **434**, 1–9.

Chappell B. and Simpson P. (1984) Source rocks of I-and S-type granites in the lachlan fold belt, Southeastern Australia [and discussion]. *Philos. Trans. Roy. Soc. Lond. A* **310**, 693–707.

Chappell B. and White A. (1974) Two contrasting granite types. *Pacific Geol.* **8**, 173–174.

Chappell B. and White A. (1992) I-and S-type granites in the Lachlan Fold Belt. *Trans. R. Soc. Edinb. Earth Sci.* **272**, 1–26.

Chappell B. and White A. J. R. (2001) Two contrasting granite types: 25 years later. *Aust. J. Earth Sci.* **48**, 489–499.

Chauvel C., Garçon M., Bureau S., Besnault A., Jahn B.-M. and Ding Z. (2014) Constraints from loess on the Hf–Nd isotopic composition of the upper continental crust. *Earth Planet. Sci. Lett.* **388**, 48–58.

Chen J., Ji J., Qiu G. and Lu H. (1998) Geochemical studies on the intensity of chemical weathering in Luochuan loess-paleosol sequence, China. *Sci. China Series D Earth Sci.-English Edition* **41**, 235–241.

Chen J.-Y., Yang J.-H., Zhang J.-H., Sun J.-F. and Wilde S. A. (2013) Petrogenesis of the Cretaceous Zhangzhou batholith in southeastern China: zircon U-Pb age and Sr–Nd–Hf–O isotopic evidence. *Lithos* **162**, 140–156.

Chen K., Walker R. J., Rudnick R. L., Gao S., Gaschnig R. M., Puchtel I. S. and Hu Z. C. (2016) Platinum-group element abundances and Re–Os isotopic systematics of the upper continental crust through time: Evidence from glacial diamictites. *Geochim. Cosmochim. Acta* **191**, 1–16.

Clarke F. W. (1889) The relative abundance of the chemical elements. *Philos. Soc. Wash. Bull. X* **1**, 131–142.

Clarke, F. W. and Washington, H. S. (1924) The composition of the earth's crust. USGS Professional Paper 127, 117pp.

Condie K. C. (1993) Chemical composition and evolution of the upper continental crust: contrasting results from surface samples and shales. *Chem. Geol.* **104**, 1–37.

Eade K. E. and Fahrig W. F. (1973) Regional, lithological, and temporal variation in the abundances of some trace elements in the Canadian shield. Geol. Sur. Canada Paper 72–46, Ottawa, Ontario, 46pp.

Ewart A. and Griffin W. L. (1994) Application of proton-microprobe data to trace-element partitioning in volcanic rocks. *Chem. Geol.* **117**, 251–284.

Field D. and Elliott R. B. (1974) The chemistry of gabbro/amphibolite transitions in south Norway. *Contrib. Mineral. Petrol.* **47**, 63–76.

Foden J., Sossi P. A. and Wawryk C. M. (2015) Fe isotopes and the contrasting petrogenesis of A-, I-and S-type granite. *Lithos* **212**, 32–44.

Foster, F. R. (1947) Glacial Geology And The Pleistocene Epoch.

Foster R. J. (1962) Precambrian corundum-bearing rocks, Madison Range, southwestern Montana. *Geol. Soc. Am. Bull.* **73**, 131–138.

Frost B. R., Barnes C. G., Collins W. J., Arculus R. J., Ellis D. J. and Frost C. D. (2001) A geochemical classification for granitic rocks. *J. Petrol.* **42**, 2033–2048.

Gallet S., Jahn B.-M., Lanoë B. V. V., Dia A. and Rossello E. (1998) Loess geochemistry and its implications for particle origin and composition of the upper continental crust. *Earth Planet. Sci. Lett.* **156**, 157–172.

Gao S., Zhang B.-R., Luo T.-C., Li Z.-J., Xie Q.-L., Gu X.-M., Zhang H.-F., Ouyang J.-P., Wang D.-P. and Gao C.-L. (1992) Chemical composition of the continental crust in the Qinling Orogenic Belt and its adjacent North China and Yangtze Cratons. *Geochim. Cosmochim. Acta* **56**, 3933–3950.

Gao S., Luo T.-C., Zhang B.-R., Zhang H.-F., Han Y.-W., Zhao Z.-D. and Hu Y.-K. (1998) Chemical composition of the continental crust as revealed by studies in East China. *Geochim. Cosmochim. Acta* **62**, 1959–1975.

Gaschnig R. M., Rudnick R. L., McDonough W. F., Kaufman A. J., Hu Z. and Gao S. (2014) Onset of oxidative weathering of continents recorded in the geochemistry of ancient glacial diamictites. *Earth Planet. Sci. Lett.* **408**, 87–99.

Gaschnig R. M., Rudnick R. L., McDonough W. F., Kaufman A. J., Valley J. W., Hu Z., Gao S. and Beck M. L. (2016) Compositional evolution of the upper continental crust through time, as constrained by ancient glacial diamictites. *Geochim. Cosmochim. Acta* **186**, 316–343.

Goldschmidt V. (1933) Grundlagen der quantitativen Geochemie. *Fortschr. Mineral. Kristallog. Petrogr.* **17**, 12.

Gong Y., Nan X., Yu H., Zeng Z. and Huang F. (2016) Barium isotope composition of a laterite profile derived from extremely weathered basalt. *Goldschm. Abstr.* **2016**, 968.

Gu Z. Y., Lal D., Liu T. S., Guo Z. T., Southon J. and Caffee M. W. (1997) Weathering histories of Chinese loess deposits based on uranium and thorium series nuclides and cosmogenic 10Be. *Geochim. Cosmochim. Acta* **61**, 5221–5231.

Gumsley A. P., Chamberlain K. R., Bleeker W., Söderlund U., de Kock M. O., Larsson E. R. and Bekker A. (2017) Timing and tempo of the Great Oxidation Event. *Natl. Acad. Sci.* **114**, 1811–1816.

Hao Q., Wang L., Oldfield F., Peng S., Qin L., Song Y., Xu B., Qiao Y., Bloemendal J. and Guo Z. (2012) Delayed build-up of Arctic ice sheets during 400,000-year minima in insolation variability. *Nature* **490**, 393–396.

Hawkesworth, C. J. and Norry, M. (1983) Continental basalts and mantle xenoliths. Shiva Pub.

Hirata T. (1996) Lead isotopic analyses of NIST standard reference materials using multiple collector inductively coupled plasma mass spectrometry coupled with a modified external correction method for mass discrimination effect. *Analyst* **121**, 1407–1411.

Horner T. J., Kinsley C. W. and Nielsen S. G. (2015) Barium-isotopic fractionation in seawater mediated by barite cycling and oceanic circulation. *Earth Planet. Sci. Lett.* **430**, 511–522.

Hsieh Y. T. and Henderson G. M. (2017) Barium stable isotopes in the global ocean: Tracer of Ba inputs and utilization. *Earth Planet. Sci. Lett.* **473**, 269–278.

Hu Z. and Gao S. (2008) Upper crustal abundances of trace elements: a revision and update. *Chem. Geol.* **253**, 205–221.

Huang Y., Chubakov V., Mantovani F., Rudnick R. L. and McDonough W. F. (2013) A reference Earth model for the heat-producing elements and associated geoneutrino flux. *Geochem. Geophys. Geosyst.* **14**, 2003–2029.

Huang F., Nan X., Hu M., Huang S. and Huang J. (2015) Barium isotope compositions of igneous rocks. *Goldschm. Abstr.* **2015**, 1331.

Kehm K., Hauri E., Alexander C. O. D. and Carlson R. (2003) High precision iron isotope measurements of meteoritic material by cold plasma ICP-MS. *Geochim. Cosmochim. Acta* **67**, 2879–2891.

Kuritani T., Ohtani E. and Kimura J.-I. (2011) Intensive hydration of the mantle transition zone beneath China caused by ancient slab stagnation. *Nat. Geosci.* **4**, 713–716.

Kurzweil F., Drost K., Pašava J., Wille M., Taubald H., Schoeckle D. and Schoenberg R. (2015) Coupled sulfur, iron and molybdenum isotope data from black shales of the Teplá-Barrandian unit argue against deep ocean oxygenation during the Ediacaran. *Geochim. Cosmochim. Acta* **171**, 121–142.

Li X.-H., Li Z.-X., Li W.-X., Liu Y., Yuan C., Wei G. and Qi C. (2007) U-Pb zircon, geochemical and Sr–Nd–Hf isotopic constraints on age and origin of Jurassic I- and A-type granites from central Guangdong, SE China: A major igneous event in response to foundering of a subducted flat-slab? *Lithos* **96**, 186–204.

Li W., Jackson S. E., Pearson N. J., Alard O. and Chappell B. W. (2009) The Cu isotopic signature of granites from the Lachlan Fold Belt, SE Australia. *Chem. Geol.* **258**, 38–49.

Li W. Y., Teng F. Z., Ke S., Rudnick R. L., Gao S., Wu F. Y. and Chappell B. W. (2010) Heterogeneous magnesium isotopic composition of the upper continental crust. *Geochim. Cosmochim. Acta* **74**, 6867–6884.

Li S., Gaschnig R. M. and Rudnick R. L. (2016) Insights into chemical weathering of the upper continental crust from the geochemistry of ancient glacial diamictites. *Geochim. Cosmochim. Acta* **176**, 96–117.

Liu T. and Ding Z. (1998) Chinese loess and the paleomonsoon. *Ann. Rev. Earth Planet Sci. Lett.* **26**, 111–145.

Loiselle M. and Wones D. R. (1979) Characteristics and origin of anorogenic granites. *Geol. Soc. Amer. Abst.* **11**, 468.

Maréchal C. N., Télouk P. and Albarède F. (1999) Precise analysis of copper and zinc isotopic compositions by plasma-source mass spectrometry. *Chem. Geol.* **156**, 251–273.

Mavromatis V., van Zuilen K., Purgstaller B., Baldermann A., Nägler T. F. and Dietzel M. (2016) Barium isotope fractionation during witherite ($BaCO_3$) dissolution, precipitation and at equilibrium. *Geochim. Cosmochim. Acta* **190**, 72–84.

McDaniel D. K., Walker R. J., Hemming S. R., Horan M. F., Becker H. and Grauch R. I. (2004) Sources of osmium to the modern oceans: new evidence from the 190Pt-186Os system1. *Geochim. Cosmochim. Acta* **68**, 1243–1252.

McDonough W. F. and Sun S. S. (1995) The composition of the Earth. *Chem. Geol.* **120**, 223–253.

McLennan S. M. (1993) Weathering and global denudation. *J. Geol.* **101**, 295–303.

McLennan, S. M. (2001) Relationships between the trace element composition of sedimentary rocks and upper continental crust. Geochem. Geophys. Geosyst. 2.

Miyazaki T., Kimura J.-I. and Chang Q. (2014) Analysis of stable isotope ratios of Ba by double-spike standard-sample bracketing using multiple-collector inductively coupled plasma mass spectrometry. *J. Anal. Atom. Spectrom.* **29**, 483.

Moynier F., Pringle E. A., Bouvier A. and Moureau J. (2015) Barium stable isotope composition of the Earth, meteorites, and calcium–aluminum-rich inclusions. *Chem. Geol.* **413**, 1–6.

Murphy D., Collerson K. and Kamber B. (2002) Lamproites from Gaussberg, Antarctica: possible transition zone melts of Archaean subducted sediments. *J. Petrol.* **43**, 981–1001.

Nan X., Wu F., Zhang Z., Hou Z., Huang F. and Yu H. (2015) High-precision barium isotope measurements by MC-ICP-MS. *J. Anal. Atom. Spectrom.* **30**, 2307–2315.

Nesbitt H. W. and Markovics G. (1980) Chemical processes affecting alkalis and alkaline earths during continental weathering. *Geochim. Cosmochim. Acta* **44**, 1659–1666.

Nesbitt H. and Young G. M. (1982a) Early Proterozoic climates and plate motions inferred from major element chemistry of lutites. *Nature* **299**, 715–717.

Nesbitt I. and Young G. (1982b) Early proterozoic climates and plate. *Nature* **299**, 21.

Nesbitt H. W. and Young G. M. (1996) Petrogenesis of sediments in the absence of chemical weathering: effects of abrasion and sorting on bulk composition and mineralogy. *Sedimentology* **43**, 341–358.

Nürnberg C. C., Bohrmann G., Schlüter M. and Frank M. (1997) Barium accumulation in the Atlantic sector of the Southern Ocean: Results from 190,000-year records. *Paleoceanography* **12**, 594–603.

Park J. W., Hu Z., Gao S., Campbell I. H. and Gong H. (2012) Platinum group element abundances in the upper continental crust revisited - New constraints from analyses of Chinese loess. *Geochim. Cosmochim. Acta* **93**, 63–76.

Paytan A. and Griffith E. M. (2007) Marine barite: Recorder of variations in ocean export productivity. *Deep Sea Res. Part II Top Stud. Oceanogr.* **54**, 687–705.

Penniston-Dorland S., Liu X. M. and Rudnick R. L. (2017) Lithium isotope geochemistry. *Rev. Mineral.Geochem.* **82**, 165–217.

Peucker-Ehrenbrink B. and Jahn B. M. (2001) Rhenium-osmium isotope systematics and platinum group element concentrations: Loess and the upper continental crust. *Geochem. Geophys. Geosyst.* **2**.

Philpotts J. A. and Schnetzler C. C. (1970) Phenocryst-matrix partition coefficients for K, Rb, Sr and Ba, with applications to anorthosite and basalt genesis. *Geochim. Cosmochim. Acta* **34**, 307–322.

Pilet S., Baker M. B., Müntener O. and Stolper E. M. (2011) Monte Carlo simulations of metasomatic enrichment in the lithosphere and implications for the source of alkaline basalts. *J. Petrol.* **52**, 1415–1442.

Plank T. and Langmuir C. H. (1998) The chemical composition of subducting sediment and its consequences for the crust and mantle. *Chem. Geol.* **145**, 325–394.

Poldervaart A. (1955) Chemistry of the earth's crust. *Geol. Soc. Am. Spec. Papers* **62**, 119–144.

Pretet C., van Zuilen K., Nägler T. F., Reynaud S., Böttcher M. E. and Samankassou E. (2015) Constraints on barium isotope fractionation during aragonite precipitation by corals. *Depositional Rec.* **1**, 118–129.

Puchelt H. (1967) Zur Geochemie des Bariums im exogenen Zyklus. *Sitzungsber. Heidelb. Akad. Math. Wiss. Nat. Kl.* **4**, 85–205.

Qi C., Deng X., Li W., Li X., Yang Y. and Xie L. (2007) Origin of the Darongshan-Shiwandashan S-type granitoid belt from southeastern Guangxi: geochemical and Sr-Nd-Hf isotopic constraints. *Acta Petrologica Sinica* **23**, 403–412.

Rehkämper M. and Mezger K. (2000) Investigation of matrix effects for Pb isotope ratio measurements by multiple collector ICP-MS: verification and application of optimized analytical protocols. *J. Anal. Atom. Spectrom.* **15**, 1451–1460.

Rehkämper M. and Halliday A. N. (1998) Accuracy and long-term reproducibility of lead isotopic measurements by multiple-collector inductively coupled plasma mass spectrometry using an external method for correction of mass discrimination. *Int. J. Mass Spectrom.* **181**, 123–133.

Roe J., Anbar A. and Barling J. (2003) Nonbiological fractionation of Fe isotopes: evidence of an equilibrium isotope effect. *Chem. Geol.* **195**, 69–85.

Ronov A. and Yaroshevsky A. (1976) A new model for the chemical structure of the Earth's crust. *Geochem. Int.* **13**, 89–121.

Rudge J. F., Reynolds B. C. and Bourdon B. (2009) The double spike toolbox. *Chem. Geol.* **265**, 420–431.

Rudnick, R. L. and Gao, S. (2014) Composition of the continental crust. Treatise on Geochemistry. 2nd. 4, pp. 1–51.

Sauzéat L., Rudnick R. L., Chauvel C., Garçon M. and Tang M. (2015) New perspectives on the Li isotopic composition of the upper continental crust and its weathering signature. *Earth Planet. Sci. Lett.* **428**, 181–192.

Savage P. S., Georg R. B., Williams H. M. and Halliday A. N. (2013) The silicon isotope composition of the upper continental crust. *Geochim. Cosmochim. Acta* **109**, 384–399.

Savage P. S., Georg R. B., Williams H. M., Turner S., Halliday A. N. and Chappell B. W. (2012) The silicon isotope composition of granites. *Geochim. Cosmochim. Acta* **92**, 184–202.

Schmitz B. (1987) Barium, equatorial high productivity, and the northward wandering of the Indian continent. *Paleoceanography* **2**, 63–77.

Shaw D., Reilly G., Muysson J., Pattenden G. and Campbell F. (1967) An estimate of the chemical composition of the Canadian Precambrian Shield. *Can. J. Earth Sci.* **4**, 829–853.

Shaw D. M., Dostal J. and Keays R. R. (1976) Additional estimates of continental surface Precambrian shield composition in Canada. *Geochim. Cosmochim. Acta* **40**, 73–83.

Smalley I. J. and Cabrera J. G. (1970) The shape and surface texture of loess particles. *Geol. Soc. Am. Bull.* **81**, 1591–1596.

Song Y., Lai Z., Li Y., Chen T. and Wang Y. (2015) Comparison between luminescence and radiocarbon dating of late Quaternary loess from the Ili Basin in Central Asia. *Quat. Geochronol.* **30**, 405–410.

Sun S. S. and McDonough W. S. (1989) Chemical and isotopic systematics of oceanic basalts: implications for mantle composition and processes. *Geol. Soc. (Lond.) Spec. Publ.* **42**, 313–345.

Taylor S., McLennan S. and McCulloch M. (1983) Geochemistry of loess, continental crustal composition and crustal model ages. *Geochim. Cosmochim. Acta* **47**, 1897–1905.

Taylor S. R. and McLennan S. M. (1985) *The continental crust: its composition and evolution*. Blackwell, Oxford, p. 312.

Teng F.-Z., McDonough W. F., Rudnick R. L., Dalpé C., Tomascak P. B., Chappell B. and Gao S. (2004) Lithium isotopic composition and concentration of the upper continental crust. *Geochim. Cosmochim. Acta* **68**, 4167–4178.

Teng F. Z. (2017) Magnesium isotope geochemistry. *Rev. Mineral. Geochem.* **82**, 219–287.

Tissot F. L. and Dauphas N. (2015) Uranium isotopic compositions of the crust and ocean: Age corrections, U budget and global extent of modern anoxia. *Geochimicaet Cosmochimica Acta* **167**, 113–143.

Tsai P.-H., You C.-F., Huang K.-F., Chung C.-H. and Sun Y.-B. (2014) Lithium distribution and isotopic fractionation during chemical weathering and soil formation in a loess profile. *J. Asian Earth Sci.* **87**, 1–10.

van Zuilen K., Müller T., Nägler T. F., Dietzel M. and Küsters T. (2016a) Experimental determination of barium isotope fractionation during diffusion and adsorption processes at low temperatures. *Geochim. Cosmochim. Acta* **186**, 226–241.

van Zuilen K., Nägler T. F. and Bullen T. D. (2016b) Barium isotopic compositions of geological reference materials. *Geostand. Geoanal. Res* **40**, 543–558.

Von Allmen K., Böttcher M. E., Samankassou E. and Nägler T. F. (2010) Barium isotope fractionation in the global barium cycle: First evidence from barium minerals and precipitation experiments. *Chem. Geol.* **277**, 70–77.

Verlag Wedepohl K. H. (1995) The composition of the continental crust. *Geochim. Cosmochim. Acta* **59**, 1217–1232.

White, W. M.,and Klein, E. M. (2014). 4.13-Composition of the Oceanic Crust. Treatise on Geochemistry (Second Edition).

Xu X., Lu W. and He Z. (2007) Age and generation of Fogang granite batholith and Wushi diorite-hornblende gabbro body. *Sci. China Series D: Earth Sci.* **50**, 209–220.

Yang J., Barling J., Siebert C., Fietzke J., Stephens E. and Halliday A. N. (2017) The molybdenum isotopic compositions of I-, S- and A-type granitic suites. *Geochim. Cosmochim. Acta* **205**, 168–186.

Ye W., Jin H., Cheng X. and Zhao X. (1998) Depositional features and material sources of loess in Yili region, Xinjiang. *Arid Land Geography* **21**, 1–8.

Zen E. A. (1986) Aluminum enrichment in silicate melts by fractional crystallization: some mineralogic and petrographic constraints. *J. Petrol.* **27**, 1095–1117.

Associate editor: Nicolas Dauphas